Mineralium Deposita (2023) 58:751–769
https://doi.org/10.1007/s00126-022-01155-7

ARTICLE

Fluid evolution and ore genesis of the Tiantangshan granite-related vein-type Rb-Sn-W deposit, south China: constraints from LA-ICP-MS analyses of fluid inclusions

Hong-Wei Peng[1,2] · Hong-Rui Fan[2,3] · Pilar Lecumberri-Sanchez[4] · Jian-Qing Lai[1] · Huan-Long Hu[2,5] · Ting-Guang Lan[3,5] · Xing-Hui Li[2]

Received: 17 January 2022 / Accepted: 2 December 2022 / Published online: 12 December 2022

Abstract

Tungsten-tin-(rare-metal) deposits are most commonly granite-related and an important source of critical metals. This study describes the fluid evolution in the Tiantangshan Rb-Sn-W deposit, Nanling Range, China, and discusses the implications for mineralizing processes. Mineralization at Tiantangshan is spatially zoned. The greisen roof hosts wolframite-cassiterite quartz veins. The surrounding volcanic rocks host biotite quartz veins (Rb mineralization) crosscut by cassiterite quartz veins and sphalerite-galena quartz veins. The earliest intermediate-density fluids are responsible for the early W-(Sn)-Rb mineralization and evolve towards decreasing homogenization temperature (Th) and ratios of W, Sn, Rb, Cs, Fe, and Mn to Na + K as the fluid migrated from the greisen to the volcanic rocks hosted veins (Th: 420 to 350 °C; salinity: 13 to 4 wt% $NaCl_{eq}$). The spatial distribution of mineralization and fluid paragenesis indicates that precipitation of wolframite, early cassiterite, and Rb-rich biotite was associated with a pH increase during fluid-rock interaction. Late cassiterite and intergrown quartz precipitated from a degassing fluid with lower Th (mainly 360 to 340 °C) and salinity (10 to 2 wt% $NaCl_{eq}$) and with distinctly lower Sn concentrations. Late cassiterite precipitation is therefore likely related with depressurization by brittle failure of the rock leading to simultaneous boiling and meteoric water input. Late Pb–Zn mineralization precipitated from low Th (< 320 °C) and salinity (0 to 2 wt% $NaCl_{eq}$) fluids through extensive mixing with meteoric water. The tempo-spatial development of Rb-Sn-W-Pb–Zn mineralization at Tiantangshan was controlled by a mixing fluid regime, where input of meteoric water gradually increased with time.

Keywords LA-ICP-MS microanalyses · Infrared microthermometry · Fluid mixing · Granite-related vein-type deposit · Tiantangshan Rb-Sn-W deposit

Introduction

Granite-related vein deposits are an important source of W and Sn in the world (Werner et al. 2014; Kamilli et al. 2017). Tungsten and Sn in these deposits typically occur in quartz-bearing veins hosted in the wallrocks surrounding a

Editorial handling: G. Beaudoin

✉ Hong-Rui Fan
fanhr@mail.iggcas.ac.cn

[1] Key Laboratory of Metallogenic Prediction of Nonferrous Metals and Geological Environment Monitoring (Ministry of Education), School of Geosciences and Info-Physics, Central South University, Changsha 410083, China

[2] Key Laboratory of Mineral Resources, Institute of Geology and Geophysics, Chinese Academy of Sciences, Beijing 100029, China

[3] College of Earth and Planetary Sciences, University of Chinese Academy of Sciences, Beijing 100049, China

[4] Department of Earth and Atmospheric Sciences, University of Alberta, Edmonton, AB T6G 2E3, Canada

[5] State Key Laboratory of Ore Deposit Geochemistry, Institute of Geochemistry, Chinese Academy of Sciences, Guiyang 550081, China

metasomatized (greisenized) granite and with a portion of mineralization located within the roof zones of the granite itself (Lehmann 1990, 2021; Černý et al. 2005; Mao et al. 2013; Romer and Kroner 2016). The fluid source and evolution and mineral precipitation mechanism in this type of deposits remain debated, particularly with respect to the source of hydrothermal fluids (Wilkinson 1990; Audétat et al. 1998; Codeço et al. 2017; Legros et al. 2020a) and the involvement of external fluids. Several studies have suggested that evolution of magmatic fluids was responsible for W-Sn mineralization, mainly during fluid cooling (Ramboz et al. 1985; Samson 1990; Ni et al. 2015; Peng et al. 2018; Yang et al. 2019a) and phase separation (Korges et al. 2018; Pan et al. 2019). In contrast, other studies stressed a critical role of fluid mixing (Heinrich 1990; Audétat et al. 1998; Wei et al. 2012; Legros et al. 2018; Pan et al. 2019; Liu et al. 2020; Harlaux et al. 2021a; Lehmann 2021), as it could cause cooling, dilution, and oxidation of hydrothermal fluids to precipitate wolframite and/or cassiterite (Heinrich 1990; Wood and Samson 2000; Schmidt 2018; Lehmann 2021). In addition, a potential role of fluid-rock interaction has also been stressed for W-Sn mineralization (Lecumberri-Sanchez et al. 2017; Harlaux et al. 2021b).

The Nanling Range is one of the largest W-Sn metallogenic provinces in the world and hosts numerous vein and skarn deposits genetically related to late Jurassic magmatism (Mao et al. 2013; Yuan et al. 2019; Wang et al. 2020; Ni et al. 2021). Rare-metal mineralization, such as Nb–Ta, Li-Be, and Rb, is also associated with the late Jurassic magmatism and W-Sn mineralization in the Nanling Range (Mao et al. 2013; Wang et al. 2020). Recent studies have focused on characterizing hydrothermal fluids responsible for W-Sn mineralization in the Nanling Range (Wei et al. 2012; Ni et al. 2015, 2020; Legros et al. 2018; Pan et al. 2019), whereas comprehensive understanding on the evolution of fluids in time and space as well as the relationship between W-Sn and rare-metal mineralization is lacking. It is possible that the current debate on the processes that cause mineralization (Wei et al. 2012; Ni et al. 2015, 2020; Legros et al. 2018; Yang et al. 2019a, b; Pan et al. 2019; Liu et al. 2020) is due to the existence of superimposed fluid events registered in quartz veins (Wilkinson 2001). Fluid paragenesis is best characterized through combination of scanning electron microscope-cathodoluminescence (SEM-CL) imaging and standard transmitted light microscopy to determine the textural relationships between mineral growth/fractures and fluid inclusions. Laser ablation-inductively coupled plasma-mass spectrometry (LA-ICP-MS) analysis of individual fluid inclusions further allows characterizing the physicochemical evolution of the fluids in the system (Landtwing et al. 2005; Klemm et al. 2008; Rottier et al. 2018; Pan et al. 2019).

The Tiantangshan deposit, located in the southeastern Nanling Range, is a Rb-Sn-W polymetallic deposit with ca. 170 kt Rb_2O, 5050 t Sn, and 4800 t WO_3 and a small amount of Pb (2600 t) and Zn (240 t). Accordingly, Tiantangshan is the largest Rb deposit in the Nanling Range and one of the largest in China (Sun et al. 2019). The most remarkable mineralizing feature of the deposit is a spatial zonation of mineralization, with Rb and Sn-W polymetallic mineralization occurring as quartz veins outwards from a greisenized granite and distal Pb–Zn mineralization, which makes Tiantangshan an excellent case study for probing into temporal and spatial fluid evolution of the W-Sn and related rare-metal mineralization. Fluids related to Sn-W mineralization at Tiantangshan have been studied in single fluid inclusions in gangue minerals and through bulk quartz oxygen isotope and inclusion fluid hydrogen isotope (Jia et al. 2018), providing information on the potential fluids present, but leaving the identification of hydrothermal fluids and the W-Sn, Rb, and Pb–Zn mineralizing processes open for further investigation.

In this study, we combine fluid inclusion petrography (including SEM-CL imaging) with physicochemical characterization of fluids in different paragenetic stages (microthermometry of fluid inclusion assemblages (FIA) and single fluid inclusion LA-ICP-MS compositional analyses) towards defining the physicochemical characteristics and evolution of hydrothermal fluids of the different mineralization stages (Rb, Sn-W, and Pb–Zn). We further propose the likely ore precipitation mechanisms for each of the mineralization stages.

Regional geological background

The Tiantangshan deposit (latitude 24°41′ N, longitude 115°22′ E) is located in the Mabugang volcanic basin, within the southeastern Nanling Range in the Cathaysia block, southeast China (Fig. 1). The basement in the Cathaysia block consists of Paleoproterozoic and Neoproterozoic rocks and was sutured with the Yangtze Block in the northwest along the Jiangnan Belt during the Neoproterozoic (Fig. 1a; Zhao and Cawood 2012). The Cathaysia block underwent multiple tectono-magmatic events from Paleozoic to Mesozoic, including the Caledonian, Indosinian, and Yanshanian orogenies. The Yanshanian period (middle-late Mesozoic) in particular is characterized by extensive granitic and volcanic rocks (Fig. 1a). The extensive Yanshanian magmatism in the Cathaysia block formed under an extensional setting in response to subduction of the paleo-Pacific plate (Zhou et al. 2006; Li and Li 2007). The Nanling Range in the middle-west of the Cathaysia block is one of the most important W-Sn districts in the world and is also known for rare-metal mineralization (Nb–Ta, Li, Be, Rb) usually accompanying the W-Sn mineralization (Mao et al. 2013; Wang et al. 2020). Large-scale W-Sn mineralization in the district is dominantly related to 160–150 Ma granitic magmatism (Mao et al. 2013; Yuan

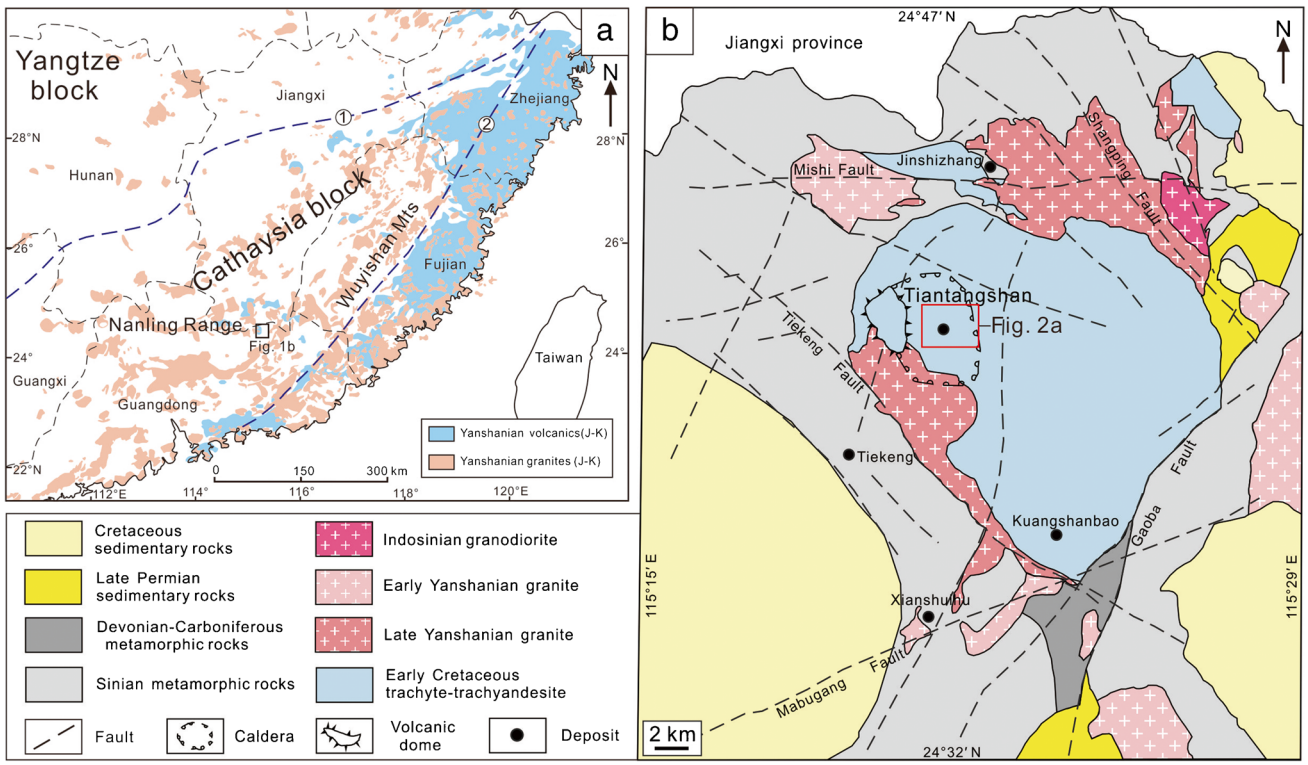

Fig. 1 **a** Simplified geological map of the southeastern China with distribution of Yanshanian granite and volcanic rocks and location of the Mabugang volcanic basin (after Zhou et al. 2006). 1: Jiangshan-Shaoxing fault; 2: Zhenghe-Dapu fault. **b** Geological map of the Mabugang volcanic basin with location of the Tiantangshan deposit (after Guo 2009)

et al. 2019; Legros et al. 2020b; Tang et al. 2020; Wang et al. 2020; Ni et al. 2021), with an early Cretaceous (145–130 Ma) Sn-dominated polymetallic metallogenic belt including the Tiantangshan deposit identified in the east-southeast Nanling Range (Liu et al. 2018, 2021; Peng et al. 2021b).

The Tiantangshan deposit is hosted in the Mabugang volcanic basin, which is bound by EW-, NE-, and NW-trending regional faults. The regional Sinian (Neoproterozoic) basement is mainly composed of gneissic-migmatitic granite and a variety of meta-sedimentary rocks (Fig. 1b). The Mabugang basin predominantly comprises intermediate to felsic ca. 137 Ma volcanic sequences (Jia et al. 2019; Peng et al. 2021a), which transition from trachytic-trachyandesitic welded tuff at the base and middle to trachydacite and rhyolitic tuff at top. In addition to the Tiantangshan deposit, Yanshanian and Indosinian granitic magmatism and mineral deposits such as the Jinshizhang silver deposit and iron deposits are present in the Mabugang basin (Fig. 1b).

Geology of the Tiantangshan deposit

The Tiantangshan Rb-Sn-W polymetallic deposit is situated in the western area of the Mabugang volcanic basin (Fig. 1b; Guo 2009). Three volcanic units outcrop in the deposit from trachydacite and rhyolite in the northwest, to trachyte-trachyandesite, to trachyte and rhyolite in the southeast (Fig. 2a). The polymetallic mineralization is genetically related to an alkali feldspar granite emplaced in the volcanic sequences of the Mabugang basin (Fig. 2d, e). The granitic stock is dominantly composed of quartz (25 ~ 35 vol%), alkali feldspar (perthite and microcline, 45 ~ 55 vol%), plagioclase (ca. 10 vol%), and biotite (ca. 10 vol%) and mainly hosted in the trachyte-trachyandesite volcanic unit (Peng et al. 2021a). The age of the alkali feldspar granite (136.2 ± 1.1 Ma) and the volcanic rocks (138.4 ± 1.2 to 136.5 ± 1.0 Ma) is similar (Jia et al. 2019; Peng et al. 2021a), which are also close to the U–Pb ages of cassiterite (133.9 ± 2.0 to 133.2 ± 1.6 Ma) and monazite associated with Rb mineralization (134.2 ± 1.8 to 132.7 ± 1.1 Ma) (Peng et al. 2021b). Chemically, the granite and the volcanic rocks have A-type affinities, with the granite having distinctly more evolved chemical features than the volcanic rocks, such as high silica (73.9 to 77.0 wt%), "seagull-like" REE pattern, and low Zr/Hf (15.0 to 20.9) and Nb/Ta (5.7 to 12.5) values (Peng et al. 2021a).

Hydrothermal alteration is pervasive in the Tiantangshan deposit and mainly includes potassic alteration and greisenization of the alkali feldspar granite, as well as biotite alteration of the volcanic wallrock. The greisen resulting from granite alteration occurs as an irregular cupola in the granite

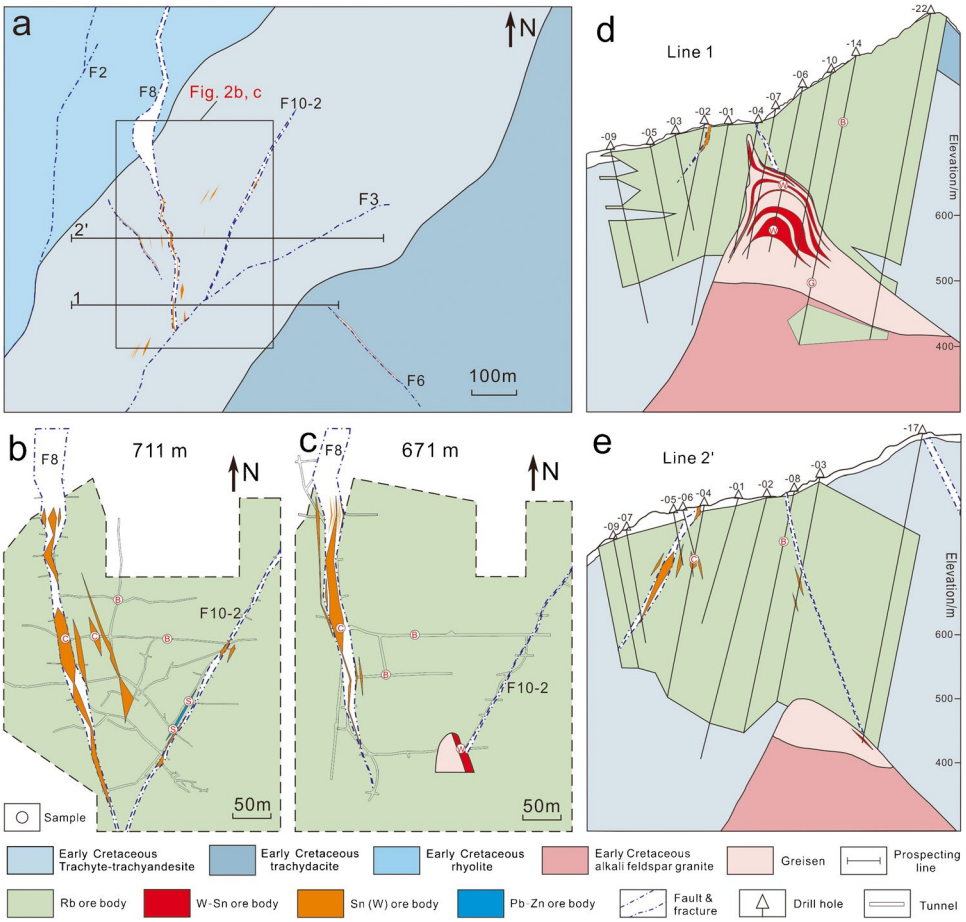

Fig. 2 Simplified geological map of the Tiantangshan deposit. **a** Plan view at surface. **b** Plan view of underground tunnel at 711 m elevation. **c** Plan view of underground tunnel at 671 m elevation. **d** Cross sections of the prospecting line 1 in **a**. **e** Cross sections of the prospecting line 2′ in **a**. The region of **b** and **c** is outlined in **a**. The Rb ore bodies within alteration zones of granite correspond to the K-feldspar alteration. Letters within circles indicating sample location: B: biotite quartz vein, C: cassiterite quartz vein, G: greisen, S: sphalerite-galena quartz vein, W: wolframite-cassiterite quartz vein

roof, which extends over 400 by 300 m in map view with thickness up to 250 m (Fig. 2d, e). The greisen mainly consists of mica (30 to 50 vol%), quartz (40 to 60 vol%), minor topaz (can be up to ca. 10 vol%), and limited pyrite (Fig. 3d), with variable overprinting chloritization. The K-feldspar alteration is transitional between the unaltered granite and the greisen and shows a discontinuous 200–400 m extent in map view and thickness up to 20–50 m (Fig. 2d). The K-feldspar alteration is characterized by high proportion of K-feldspar (≥ 60 vol%; Peng et al. 2021b). The volcanic wallrocks at the contact with the granite and greisen are aphanitic black to purple black and metamorphosed to hornfels (Peng et al. 2021b). Biotite alteration of the volcanic wallrocks develops outwards from the greisen (Fig. 2d, e) and is associated with quartz veins radiating from the greisen and crosscutting the volcanic rocks (Fig. 3a, g; Peng et al. 2021b). Biotite occurs as small crystal flakes in quartz vein selvages and volcanic rocks (Figs. 3g and 4d, e), and the intensity of biotite alteration decreases with increasing distance from the quartz veins (Fig. 3g). The biotite alteration corresponds to the major Rb mineralization of the deposit and covers a large volume of 500 east–west by 400 north–south with variable thickness up to ca. 300 m (Fig. 2).

The spatial distribution of W and minor Sn mineralization at Tiantangshan is dominantly correlated with the granite cupola (greisen), while Sn and Pb–Zn mineralization is mainly controlled by the F8 and F10-2 shallow fracture zones (Fig. 2). The F8 fracture zone extends NNW for ca. 750 m and dips west at 55 to 80°, and the F10-2 fracture zone extends NE for ca. 450 m and dips SE at 65 to 75°. The volcanic wallrock in the two fracture zones is intensively altered by silica and biotite alteration.

Polymetallic mineralization of the Tiantangshan deposit dominantly occurs in quartz veins containing wolframite-cassiterite (W-Sn), biotite (Rb), cassiterite (Sn), and sphalerite-galena (Pb–Zn). The different vein types systematically occur in different areas of the deposit (Fig. 2). The wolframite-cassiterite quartz veins are restricted to the greisen roof and inner contact zone with volcanic wallrocks (Fig. 2c–e) and have no obvious crosscutting relationship with the quartz veins of Rb, Sn, and Pb–Zn mineralization hosted in the volcanic rocks. The W-Sn ore bodies include W resources of 4800 t WO_3 at an average grade of 0.26% and minor Sn resources of 1850 t at an average grade of 0.32%. Rubidium mineralization is dominantly hosted in the volcanic rocks (Fig. 2) and corresponds to the biotite quartz veins and related biotite alterations of volcanic

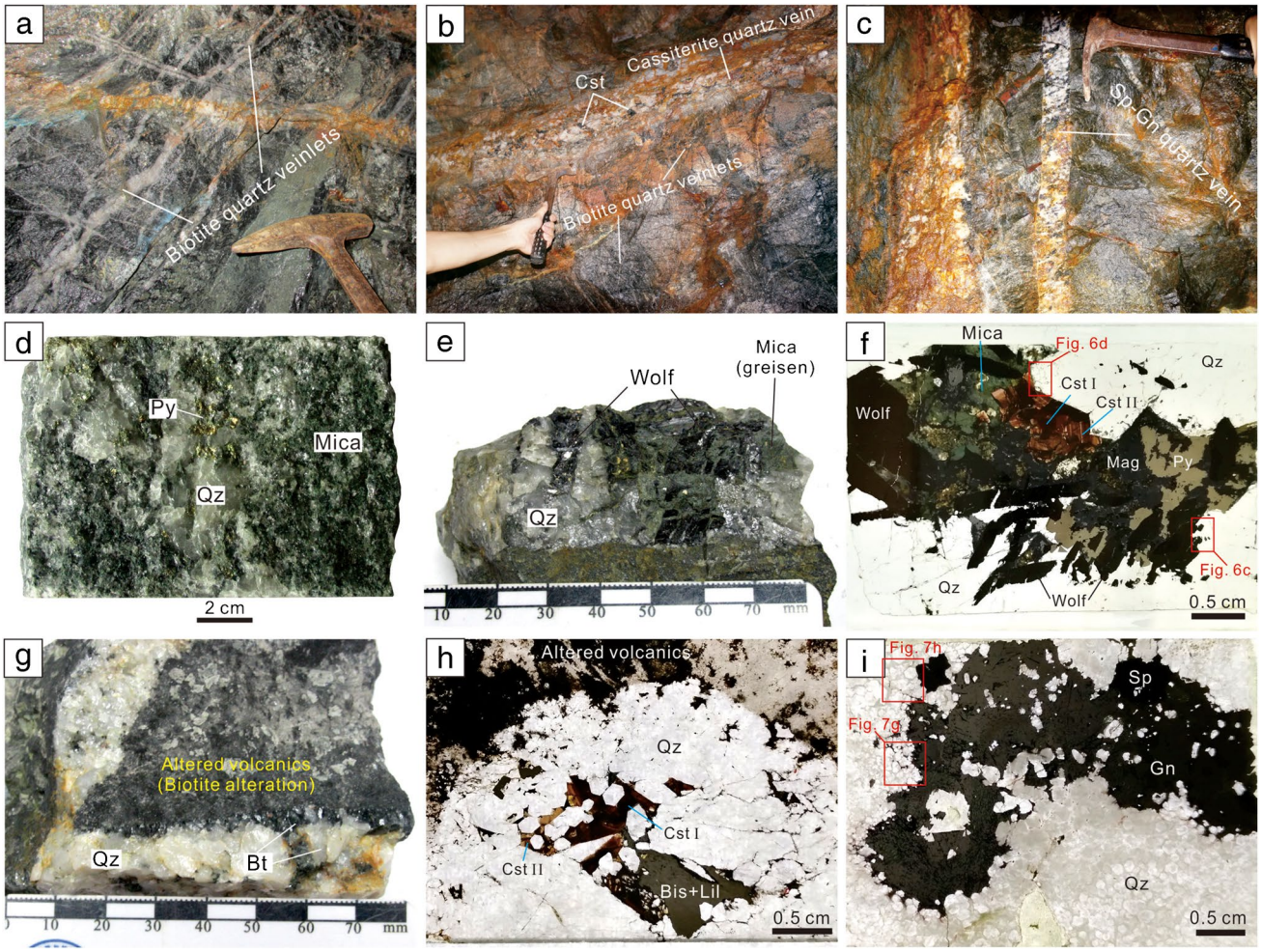

Fig. 3 Representative photographs showing different stages of mineralization and quartz veins from the Tiantangshan deposit. **a** Biotite quartz veinlets, **b** cassiterite quartz veins, and **c** sphalerite-galena quartz veins, hosted in volcanic rocks. **d** Specimen of greisen with quartz, mica, and limited pyrite. **e** Specimen of wolframite-cassiterite quartz vein. **f** Photomicrograph of wolframite-cassiterite quartz vein showing wolframite and two stages of cassiterite overgrown by pyrite and magnetite. **g** Specimen of biotite quartz vein with biotite alteration of volcanic rocks. **h** Photomicrograph of cassiterite quartz vein showing two stages of cassiterite overgrown by bismuthinite and lillianite. **i** Photomicrograph of sphalerite-galena quartz vein showing intergrown sphalerite and galena in quartz. Bis: bismuthinite, Bt: biotite, Cst: cassiterite, Gn: galena, Lil: lillianite, Mag: magnetite, Mol: molybdenite, Py: pyrite, Qz: quartz, Sp: sphalerite, Wolf: wolframite

rocks (Fig. 3a, g), with reserves of 169,000 t Rb_2O at an average grade of 0.12%, where Rb is hosted in biotite (0.4 to 1.3 wt%) through substitution of K (Han et al. 2021). The biotite quartz veins are hosted in the volcanic rocks and spatially distal from the greisen compared to wolframite-cassiterite quartz veins. The biotite quartz veins are 1 to 7 cm veins in areas proximal to the contact zone with the greisen and disseminated veinlets in peripheral areas (Fig. 3a, g). A small amount of Rb mineralization is also hosted by the K-feldspar alteration of the granite with 4400 t Rb_2O at an average grade of 0.11% (Fig. 2d), where the whole rocks have 1992 to 2092 ppm Rb (Peng et al. 2021b) and the K-feldspar minerals have 2000 to 3500 ppm Rb (Han et al. 2021). The major Sn mineralization hosted in the volcanic rocks occurs as cassiterite quartz veins with estimated reserves of 3200 t Sn at an average grade of 0.46% in a continuous ore body up to ca. 200 m along dip in the F8 fault and in discrete smaller bodies in the F10-2 fault (Fig. 2). The Pb–Zn mineralization occurs as sphalerite-galena quartz veins also in F8 and F10-2 (Figs. 2b and 3i) and includes resources of 2600 t Pb and 240 t Zn. The biotite quartz veins are crosscut by the cassiterite quartz vein and more distally by the sphalerite-galena quartz vein (Fig. 3b, c).

Sampling and analytical methods

Sampling strategy and SEM-CL

Representative ore samples of the greisen and wolframite-cassiterite quartz were collected from drill holes at

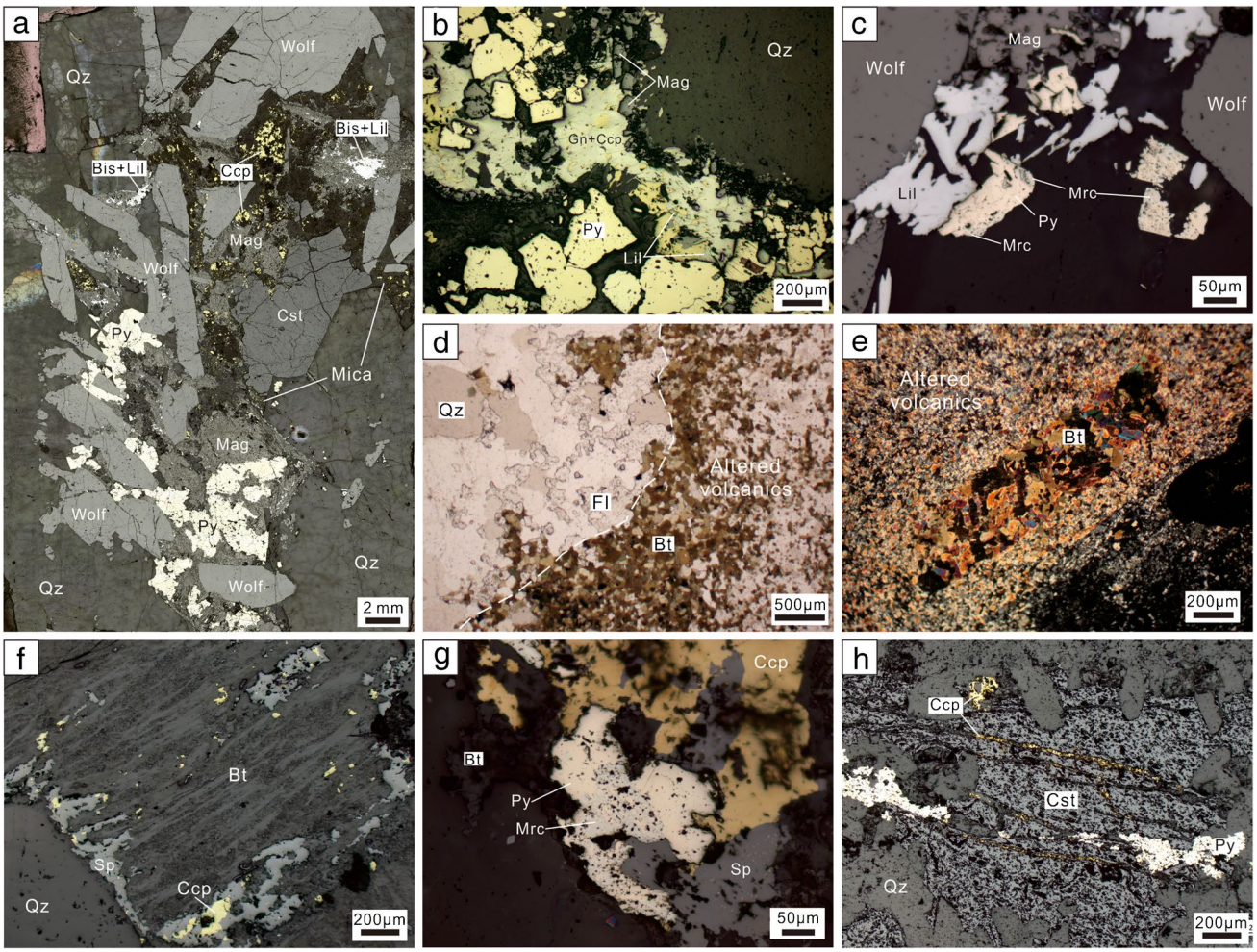

Fig. 4 Photomicrographs showing mineral assemblages of the wolframite-cassiterite quartz vein (**a–c**), biotite quartz vein (**d–g**), and cassiterite quartz vein (**h**) from the Tiantangshan deposit. **a** Wolframite-cassiterite quartz vein with location in Fig. 3f showing wolframite and cassiterite overgrown by magnetite, pyrite, chalcopyrite, bismuthinite, and lillianite. **b** Euhedral pyrite and magnetite cemented by galena, lillianite, and chalcopyrite. **c** Marcasite replacing pyrite associated with lillianite. **d** Biotite and fluorite at the edge of veins and into volcanic wallrocks. **e** Biotite replacing a plagioclase phenocryst in volcanic wallrock. **f** Sphalerite and chalcopyrite overgrowing or replacing biotite. **g** Marcasite replacing pyrite associated with sphalerite and chalcopyrite in biotite quartz vein. **h** Pyrite and chalcopyrite replacing cassiterite. Bis: bismuthinite, Bt: biotite, Ccp: chalcopyrite, Cst: cassiterite, Fl: fluorite, Gn: galena, Lil: lillianite, Mag: magnetite, Mrc: marcasite, Py: pyrite, Qz: quartz, Sp: sphalerite, Wolf: wolframite

prospecting lines of 1, 3′, and 7 and partly from a tunnel at elevation of 671 m (Fig. 2). Representative ore samples of the biotite, cassiterite, and sphalerite-galena quartz veins were mainly collected from tunnels at elevations of 671 and 711 m and partly from drill holes along the 1 and 2′ prospecting lines (Fig. 2). Doubly polished sections for fluid inclusion study were made at ca. 100 μm thickness for opaque minerals (wolframite and sphalerite) and 200 to 300 μm thickness for transparent to translucent minerals (quartz, cassiterite, topaz, and fluorite). Over 120 sections were examined for petrographic observations, and 24 of them were selected for microthermometry and LA-ICP-MS analysis of fluid inclusions. The descriptions and location of samples are given in ESM Table S1.

Quartz and cassiterite were imaged using a TESCAN MIRA3 field-emission SEM at the Guangzhou Tuoyan Testing Technology Co., Ltd. Cathodoluminescence (CL) imaging was performed using an accelerating voltage of 20 kV and a primary beam current of 15 nA.

Petrography and microthermometry of fluid inclusions

Fluid inclusion petrography was carried out under visible and infrared transmitted light using an Olympus BX53 infrared (IR) microscope at the Institute of Geology and Geophysics, Chinese Academy of Sciences (IGGCAS), coupled with a QImaging Retiga-2000R digital CCD camera.

Microthermometry of fluid inclusions was conducted using a Linkam THMSG 600 heating/freezing stage mounted on the IR microscope. The stage was calibrated with synthetic pure H_2O quartz fluid inclusion standards to ± 0.1 °C at 0 °C and ± 2 °C at 374 °C. We conducted heating first, followed by cooling, and the heating/cooling rate was set to ca. 10 °C/min and reduced to 1 to 0.1 °C/min when close to phase changes of fluid inclusions. To avoid the "warming effect" from IR light on microthermometric results of the fluid inclusions in wolframite and sphalerite (Moritz 2006; Casanova et al. 2018; Peng et al. 2020), temperatures of ice melting (Tm) were measured using the improved cycling method (Peng et al. 2020), and homogenization temperatures (Th) were obtained under the lowest possible IR light intensity with the smallest diaphragm size (Moritz 2006; Peng et al. 2020).

LA-ICP-MS analysis of individual fluid inclusion

Fluid inclusion compositions were measured through LA-ICP-MS at the State Key Laboratory of Ore Deposit Geochemistry, Institute of Geochemistry, Chinese Academy of Sciences, following the procedure described in Lan et al. (2017, 2018). The analytical instrument comprises an Agilent 7900 ICP-MS connected with a GeoLasPro 193 nm ArF excimer laser. Samples were placed in a small ablation cell to improve the washout efficiency. During ablation, the laser system was set to a repetition rate of 8 Hz and energy density of 10 J/cm^2, and laser spot sizes ranging from 16 to 44 µm were used, depending on the size of inclusions. Helium was used as carrier gas with 3 ml/min N_2 added to increase the sensitivity, which then was mixed with argon via a T-connector before entering the ICP. The dwell time for the concerned elements (^{23}Na, ^{39} K, ^{55}Mn, ^{57}Fe, ^{66}Zn, ^{85}Rb, ^{118}Sn, ^{133}Cs, ^{182} W, and ^{208}Pb) was set to 8 ms, with a total dwell time of 270 ms. The NIST SRM610 was used as the external standard and was analyzed twice every 10 analyses. The sodium content obtained from microthermometric salinities of fluid inclusions (wt% NaCl equivalent) was used as the internal standard for elemental concentrations of fluid inclusion (Heinrich et al. 2003). Hosting correction was performed using an internal standard of 15.4 wt% Si for topaz measured by EPMA and of 100 wt% SiO_2 for quartz. The raw data from the LA-ICP-MS were processed using the SILLS software (Guillong et al. 2008).

Results

Vein and paragenetic sequences

Granite-hosted mineralization in the Tiantangshan deposit consists of a K-feldspar alteration zone overprinted by greisenization and crosscut by the wolframite-cassiterite quartz veins. In the veins, euhedral tabular wolframite (up to centimeter in length) is spatially associated with the greisen mica (Figs. 3e, f and 4a). Cassiterite occurs as subhedral crystals and is light brown to dark brown in color with oscillatory growth textures showing white and brown bands (Figs. 3f and 4a). Quartz in the veins overgrows and crosscuts wolframite, but is euhedral in contact with cassiterite (Figs. 3f and 4a). In addition, magnetite, pyrite, native bismuth, and Bi-sulfide minerals (bismuthinite and lillianite) with limited arsenopyrite, chalcopyrite, galena, and sphalerite commonly overgrow and crosscut wolframite and cassiterite (Figs. 3f and 4a, b). Within these sulfide-dominated associations, pyrite and magnetite have ambiguous paragenetic relationships, but they are both commonly overgrown by later bismuthinite, lillianite, galena, and sphalerite (Fig. 4a, b), and pyrite is partly replaced by marcasite (Fig. 4c).

The volcanic rock-hosted mineralization of the Tiantangshan deposit includes extensive biotite quartz veins crosscut by cassiterite and sphalerite-galena quartz veins (Fig. 3a–c). Biotite quartz veins consist of coarse euhedral biotite usually distributed along vein walls (Fig. 3g) and fine-grained biotite replacing the matrix and pseudomorphing plagioclase phenocrysts within the trachyte-trachyandesite wallrocks (Fig. 4d, e). Fluorite and molybdenite are also common in the vein selvage intergrown with biotite (Fig. 4d). Minor pyrite, sphalerite, chalcopyrite, bismuthinite, and lillianite occur in the vein overgrowing and/or replacing biotite (Fig. 4f, g), with pyrite partly replaced by marcasite (Fig. 4g). Cassiterite quartz veins hosted in the volcanic rocks are paragenetically similar to wolframite-cassiterite quartz veins hosted in the greisen roof (Fig. 5). The main difference is that cassiterite quartz veins lack the wolframite mineralization stage. The euhedral to subhedral cassiterite in this vein also has oscillatory zoning (Fig. 3h) and is overgrown and crosscut by bismuthinite, lillianite, pyrite, chalcopyrite, etc. (Figs. 3h and 4h). Sphalerite-galena quartz veins consist of dominantly early euhedral quartz overgrown by galena and sphalerite with accessory fluorite, chalcopyrite, arsenopyrite, and pyrite (Fig. 3i). The paragenetic sequences of K-feldspar alteration to greisen and the different quartz veins are summarized in Fig. 5.

Textures of quartz and cassiterite under SEM-CL

Quartz in the greisen consists of irregular CL-bright homogeneous cores overgrown by CL-dark irregular zoned rims (Fig. 6a). Quartz in the wolframite-cassiterite quartz veins consists of an early CL-bright zoned generation (Qz_w-1) that overgrows and postdates wolframite (Fig. 6c, e), but exhibits straight boundaries and likely

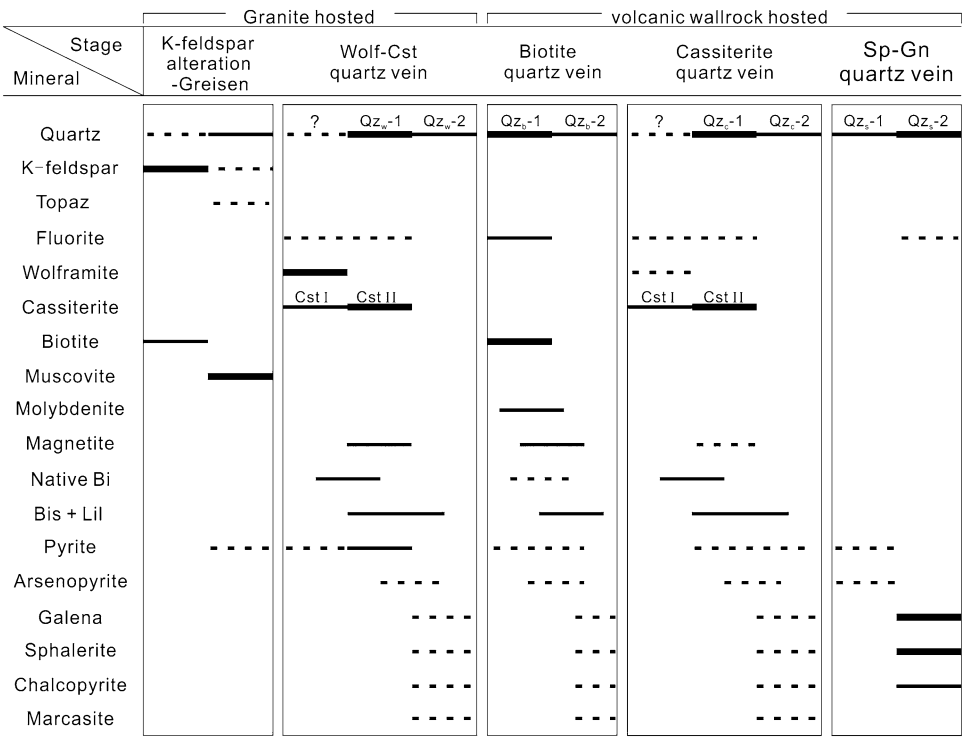

Fig. 5 Schematic paragenetic sequence of different mineralizing stages of the Tiantangshan deposit. Bis: bismuthinite, Cst: cassiterite, Gn: galena, Lil: lillianite, Qz: quartz, Sp: sphalerite, Wolf: wolframite

coprecipitated with cassiterite (Fig. 6d). The early quartz generation (Qz_w-1) is overgrown and crosscut by thin veinlets of a dull-CL homogeneous generation (Qz_w-2).

Quartz in biotite quartz veins (Qz_b) consists of an early homogeneous bright-CL quartz (Qz_b-1) coprecipitated with biotite, which is crosscut or overgrown by a Qz_b-2 generation of homogeneous, dull-CL quartz (Fig. 7a; ESM Fig. S1). The cassiterite quartz vein also has two quartz generations with the same characteristics as the wolframite-cassiterite quartz vein: a CL-bright zoned euhedral Qz_c-1 intergrown with cassiterite and a dull-CL homogeneous Qz_c-2 crosscutting Qz_c-1 in veinlets (Fig. 6i, j). Quartz in sphalerite-galena quartz veins consists of an early euhedral zoned bright-CL Qz_s-1 infilled by fine-grained dull-CL Qz_s-2 coprecipitating with sphalerite and galena (Fig. 7g, h).

Cassiterite from the wolframite-cassiterite and cassiterite quartz veins similarly consists of two generations. The early generation dark-brown cassiterite with dull and homogeneous CL feature (Cst I) is overgrown and locally replaced by the late cassiterite generation (Cst II), which is characterized by bright CL zonation texture (Figs. 3f, h and 6i).

Petrography and microthermometric results of fluid inclusions

Fluid inclusions in greisen and different stages of quartz veins in the Tiantangshan deposit are dominantly two-phase liquid-rich fluid inclusions and less frequently vapor-rich inclusions. Exceptionally, three-phase CO_2-rich fluid inclusions and three-phase fluid inclusions containing solid crystals (halite) are observed in quartz, but they are scarce and isolated, without consistent phase ratio and/or microthermometric behaviors, and therefore cannot be interpreted in a FIA framework. During microthermometric measurements, phase changes of CO_2 (melting temperatures of CO_2 and clathrate and Th_{CO2}) were not observed in most fluid inclusions. The eutectic melting, when observed, was mainly ranging from − 22 to − 20 °C, indicating a NaCl-H_2O ± KCl dominated system (Goldstein and Reynolds 1994). Therefore, the salinity was calculated using the HokieFlincs_H_2O-NaCl program (Steele-MacInnis et al. 2012). The thermometric results for all the fluid generations in the Tiantangshan deposit are presented in ESM Table S2.

The highest homogenization temperatures and salinities in the Tiantangshan deposit are recorded in fluid inclusions hosted in topaz and wolframite within greisen. The two-phase liquid-rich intermediate-density (ID) fluid inclusions in topaz are relatively large in size (20 to 60 μm in diameter) with elliptical shape and occur in groups without clear primary or secondary relationships (Goldstein and Reynolds 1994) but show consistent volume ratio of vapor phase (ca. 40 to 50 vol%; Fig. 6b). The inclusions in topaz have consistent ranges in Th from 420 to 395 °C and salinity from 9.1 to 11.0 wt% $NaCl_{eq}$ (Fig. 8a). Fluid inclusions in greisen quartz lack consistent fluid phase ratios or petrographic relationships, and therefore, their study was not pursued further. The primary fluid inclusion

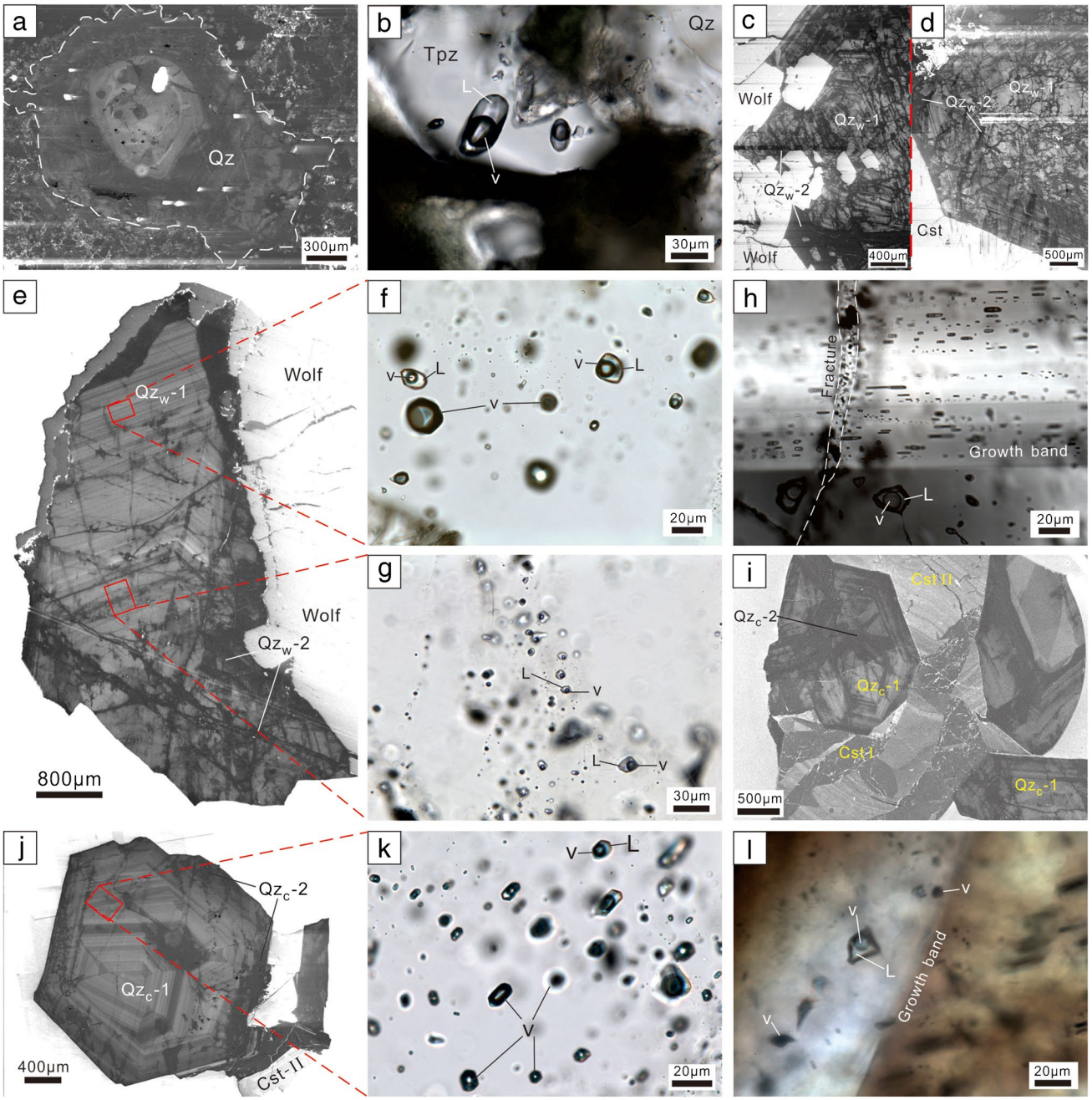

Fig. 6 **a** Quartz in greisen under SEM-CL imaging with bright-CL core and dark-CL overgrowth. **b** Liquid-rich ID fluid inclusions in greisen topaz. **c** Bright-Cl zoned Qz_w-1 encompassing wolframite and crosscut by dark-CL Qz_w-2 in wolframite-cassiterite quartz veins with location indicated in Fig. 3f. **d** Bright-Cl zoned Qz_w-1 in contact with cassiterite and crosscut by dark-CL Qz_w-2 in wolframite-cassiterite quartz veins with location indicated in Fig. 3f. **e** Bright-Cl zoned Qz_w-1 crosscut by dark-CL Qz_w-2 in wolframite-cassiterite quartz veins. **f** Coexisting liquid-rich and vapor inclusions in the Qz_w-1 with location indicated in **e**. **g** Liquid-rich FIA in the Qz_w-2 with location indicated in **e**. **h** Liquid-rich ID FIA in wolframite from the wolframite-cassiterite quartz vein, parallel to growth bands of wolframite. **i** SEM-CL image showing relationships of early and late cassiterite with Qz_c-1 and Qz_c-2 in cassiterite quartz vein. **j** SEM-CL image of euhedral quartz intergrown with cassiterite in the cassiterite quartz vein. **k** Coexisting liquid-rich and vapor inclusions in the Qz_c-1 with location indicated in **j**. **l** Coexisting liquid-rich and vapor inclusions in the late cassiterite from the cassiterite quartz vein. Cst: cassiterite, Qz: quartz, Tpz: topaz, Wolf: wolframite

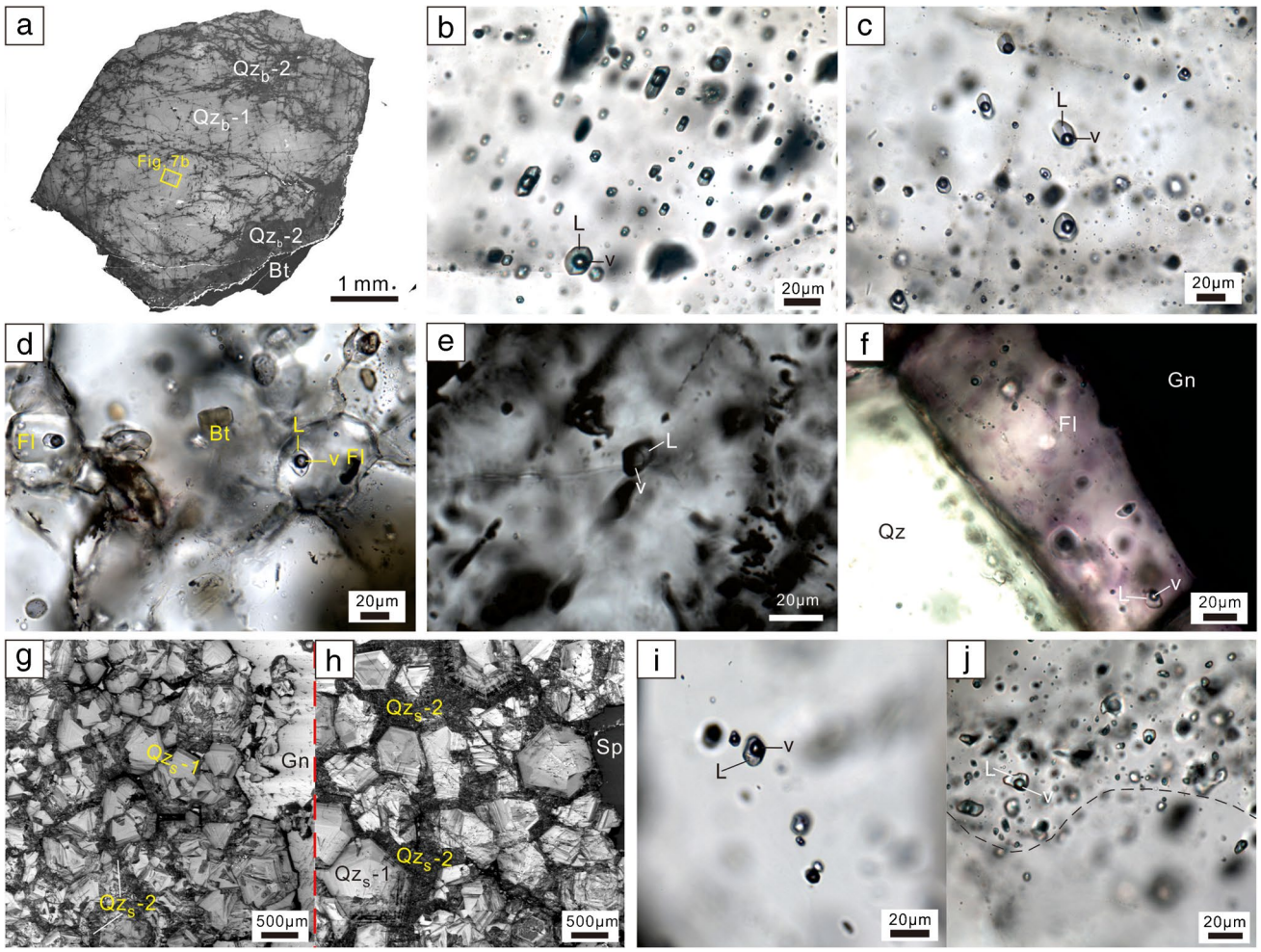

Fig. 7 **a** SEM-CL image of quartz intergrown with biotite in the biotite quartz vein, comprising Qz_b-1 intersected by Qz_b-2. **b** Liquid-rich ID FIA in the Qz_b-1 with location indicated in **a**. **c** Liquid-rich FIA in Qz_b-2 from biotite quartz vein with location indicated in ESM Fig. S1. **d** Liquid-rich ID fluid inclusions in fluorite intergrown with biotite in biotite quartz vein. **e** Liquid-rich fluid inclusion in sphalerite from the sphalerite-galena quartz vein, under infrared light. **f** Liquid-rich fluid inclusions in fluorite associated with galena. **g** CL images of Qz_s-1 and Qz_s-2 associated with galena with location identified in Fig. 3i. **h** CL images of Qz_s-1 and Qz_s-2 associated with sphalerite with location identified in the Fig. 3i. **i** Liquid-rich ID FIA in Qz_s-1. **j** Liquid-rich fluid inclusions in Qz_s-2. Bt: biotite, Fl: fluorite, Gn: galena, Qz: quartz

assemblages (FIAs) hosted in wolframite growth zones within the wolframite-cassiterite quartz veins consist of two-phase liquid-rich ID inclusions with vapor volume ratio of ca. 40 to 50 vol% and rounded to polygonal shape with diameters of 10–30 μm (Fig. 6h). These FIAs have Th from 417 to 398 °C and salinities from 10.1 to 12.7 wt% $NaCl_{eq}$ (Fig. 8a), which are comparable in Th and salinity with the inclusions in topaz.

Slightly lower fluid temperatures and salinities are recorded in wolframite-cassiterite quartz veins (hosted in greisen) and in biotite, cassiterite, and sphalerite-galena quartz veins (hosted in volcanic rocks). In wolframite-cassiterite quartz veins and cassiterite quartz veins, these lower temperature and salinity two-phase liquid-rich inclusions with ca. 40 vol% vapor phase coexist with vapor-rich fluid inclusions (commonly > 90 vol% vapor phase) forming FIAs. Within wolframite-cassiterite quartz veins, the fluid inclusions include (1) scarce isolated two-phase liquid-rich fluid inclusions in cassiterite with Th from 376 to 344 °C and salinities from 5.0 to 9.3 wt% $NaCl_{eq}$ (Fig. 8a) and (2) primary or pseudosecondary FIAs distributed along growth zones or ending at the internal growth bands of Qz_w-1 (Fig. 6e, f) with Th ranging from 366 to 343 °C and variable salinities from 2.1 to 11.7 wt% $NaCl_{eq}$ (Fig. 8a). In biotite quartz veins, two populations of two-phase liquid-rich fluid inclusions with 40 to 50 vol% vapor phase are comparable in terms of thermometry: (1) isolated inclusions in fluorite with consistent vapor ratios having Th from 377 to 360 °C and salinities from 5.9 to 8.0 wt% $NaCl_{eq}$ (Figs. 7d and 8b) and (2) primary or pseudosecondary clusters and FIA trails in

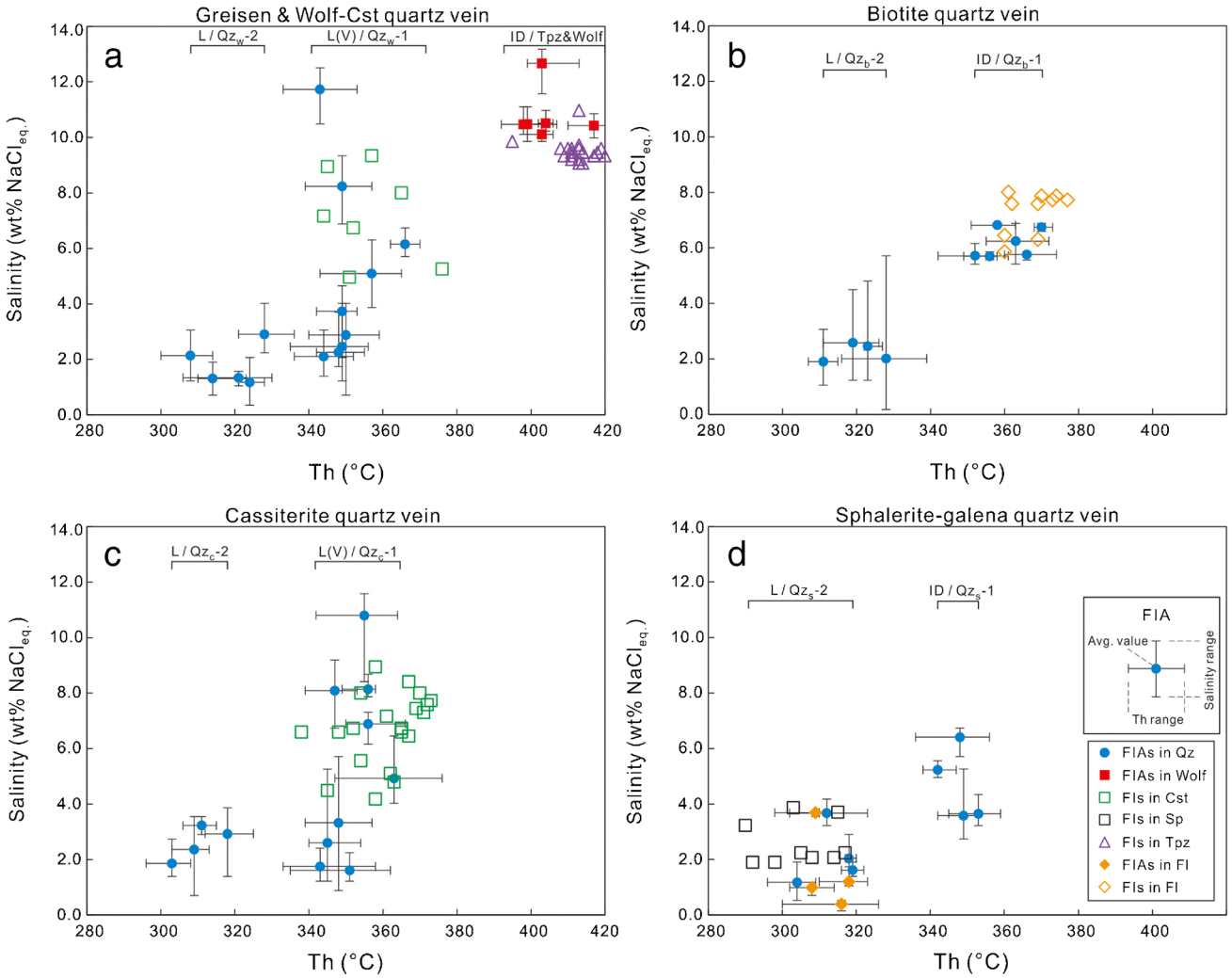

Fig. 8 Plots of homogenization temperature (Th) vs. salinity for fluid inclusion assemblages from different mineralization stages at the Tiantangshan deposit. **a** Greisen and wolframite-cassiterite quartz vein. **b** Biotite quartz vein. **c** Cassiterite quartz vein. **d** Sphalerite-galena quartz vein. Fluid inclusion type: ID: liquid-rich intermediate-density inclusion, L(V): liquid-rich inclusion in boiling FIA, L: liquid-rich inclusion, Cst: cassiterite, Fl: fluorite, Qz: quartz, Sp: sphalerite, Tpz: topaz, Wolf: wolframite

Qz_b-1 unrelated to Qz_b-2 (Fig. 7a, b) having Th from 370 to 352 °C and salinities from 5.7 to 6.8 wt% $NaCl_{eq}$ (Fig. 8b). Within the cassiterite quartz vein, two populations of fluid inclusions are of comparable thermometry: (1) scarce isolated two-phase liquid-rich fluid inclusions dominant in cassiterite or locally coexisting with liquid-rich and vapor-rich inclusions along growth bands in cassiterite (Fig. 6l) have Th from 373 to 338 °C and salinities from 4.2 to 9.0 wt% $NaCl_{eq}$ (Fig. 8c), and (2) primary or pseudosecondary fluid inclusion clusters including both vapor- and liquid-rich inclusions, mainly along growth bands of Qz_c-1 (Fig. 6j, k), have Th from 363 to 343 °C and salinities from 1.6 to 10.8 wt% $NaCl_{eq}$ (Fig. 8c). In sphalerite-galena quartz vein, FIAs with ca. 40 vol% vapor phase hosted in growth zones within Qz_s-1 (Fig. 7i) have Th ranging from 353 to 342 °C and salinities from 3.6 to 6.4 wt% $NaCl_{eq}$ (Fig. 8d).

Secondary two-phase liquid-rich fluid inclusions commonly occur as inclusion trails crosscutting early quartz (Qz_w-1, Qz_b-1, and Qz_c-1) along with the secondary dull CL quartz (i.e., Qz_w-2, Qz_b-2, and Qz_c-2) (Figs. 6e, g, i, j and 7a, c; ESM Fig. S1), which have low vapor phase volume ratio (ca. 20 to 30 vol%) and "negative crystal" shapes (Figs. 6g and 7c). These FIAs have Th and salinity ranges of 328 to 308 °C and 1.2 to 2.9 wt% $NaCl_{eq}$ for the wolframite-cassiterite quartz vein (Fig. 8a), 328 to 311 °C and 1.9 to 2.6 wt% $NaCl_{eq}$ for the biotite quartz vein (Fig. 8b), and 318 to 303 °C and salinities from 1.9 to 3.2 wt% $NaCl_{eq}$ for the cassiterite quartz vein (Fig. 8c). Meanwhile, the fluid inclusions in sphalerite-galena quartz vein with similar petrographic characters and thermometric properties include (1) isolated fluid inclusions in sphalerite with Th from 317 to 290 °C and salinities from 1.9 to 3.9 wt% $NaCl_{eq}$ (Figs. 7e and 8d),

(2) FIAs in fluorite with Th from 318 to 308 °C and salinities from 0.4 to 3.7 wt% $NaCl_{eq}$ (Figs. 7f and 8d), and (3) pseudosecondary FIAs hosted in Qz_s-2 overgrowing Qz_s-1 with Th from 319 to 304 °C and salinities from 1.2 to 3.7 wt% $NaCl_{eq}$ (Figs. 7j and 8d).

Composition of fluid inclusions

Fluid inclusions from greisen and different stages of quartz veins in the Tiantangshan deposit contain abundant Na as major component (> 1 wt%) and variable K at major to trace level (< 0.1 wt%, i.e., < 1000 ppm). Most inclusions contain variable concentrations of Fe and Mn at minor (1 to 0.1 wt%) to trace level and W, Sn, Pb, Zn, Rb, and Cs at trace level. Representative laser-ablation signals of these elements for fluid inclusions from different veins and stages are shown in ESM Fig. S2, and the LA-ICP-MS elemental concentration results of fluid inclusion are listed in ESM Table S3.

The liquid-rich ID fluid inclusions in topaz hosted in greisen have relatively high concentrations of 23 ppm W, 200 ppm Sn, 550 ppm Rb, 270 ppm Cs, 450 ppm Pb, 800 ppm Zn, 6800 ppm Fe, and 2500 ppm Mn in average (ESM Table S3; Fig. 9). By comparison, the liquid-rich ID inclusions in biotite quartz veins (Qz_b-1) and sphalerite-galena quartz veins (Qz_s-1) have low concentration of W mostly below detection limits (average $\bar{x}$ = 1.5 ppm), one order of magnitude lower concentration of Sn (46 ppm to below detection limit), Rb ($\bar{x}$ = 93 ppm), and Cs ($\bar{x}$ = 59 ppm), comparable but slightly lower Pb and Zn at hundreds ppm level (ESM Table S3; Fig. 9). Similarly, liquid-rich inclusions within FIAs in Qz_w-1 of the wolframite-cassiterite quartz vein and Qz_c-1 of the cassiterite quartz vein have highly variable but overall low concentrations of ore elements, dominantly below detection limits except for Rb ($\bar{x}$ = 51 ppm) and Cs ($\bar{x}$ = 44 ppm) (ESM Table S3; Fig. 9).

Late low-Th and low-salinity liquid-rich FIAs in wolframite-cassiterite quartz veins (Qz_w-2), biotite quartz veins (Qz_b-2), cassiterite quartz veins (Qz_c-2), and sphalerite-galena quartz veins (Qz_s-2) have concentrations of ore elements mostly below detection limit except for Rb ($\bar{x}$ = 65 ppm) and Cs ($\bar{x}$ = 35 ppm) (ESM Table S3; Fig. 9).

Discussion

Early-stage mineralization: W, Sn, and Rb

Paragenetically, the earliest fluids identified in the system are those responsible for wolframite precipitation at the greisen roof (wolframite-cassiterite quartz veins; Figs. 2 and 5). These fluids are represented by single-phase intermediate-density (ID) fluids in both wolframite and

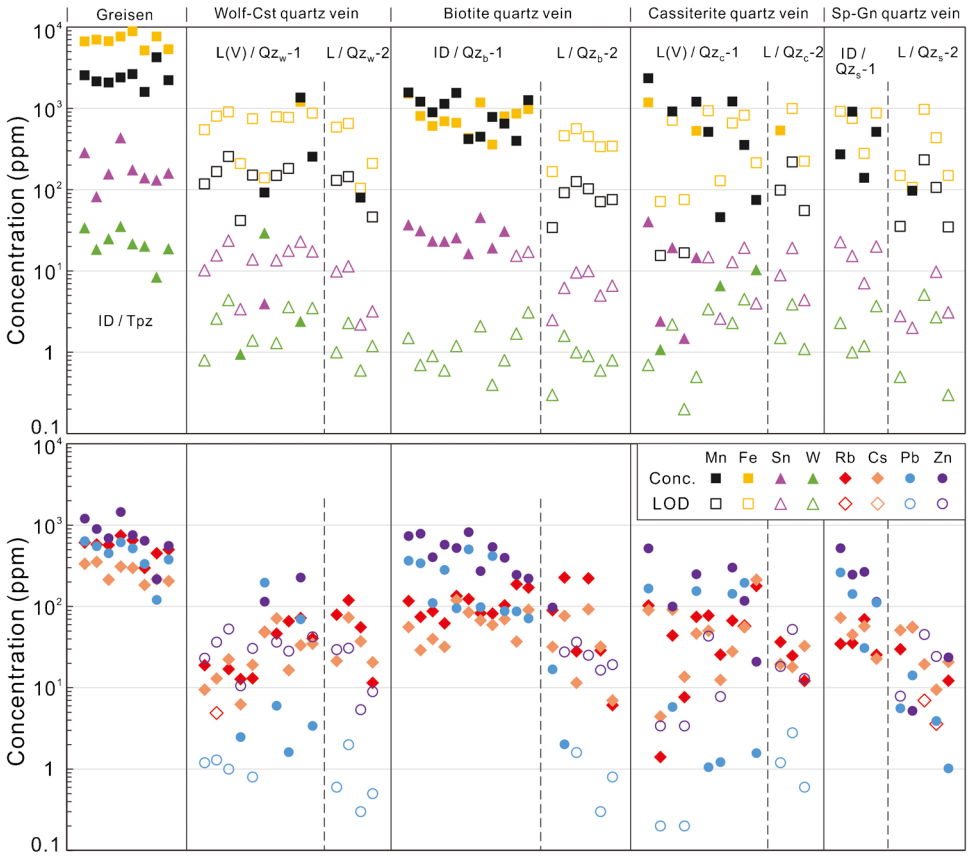

Fig. 9 Elemental concentrations of fluid inclusions hosted in topaz from greisen and quartz from different quartz veins. Fluid inclusions where the concentration is below detection limit are indicated by open symbols using the values of LOD. Conc.: concentration, LOD: limit of detection, fluid inclusion type: ID: liquid-rich intermediate-density inclusion, L(V): liquid-rich inclusion in boiling FIA, L: liquid-rich inclusion, Cst: cassiterite, Gn: galena, Qz: quartz, Sp: sphalerite, Wolf: wolframite

topaz within greisen and with comparable thermometric properties (Th from 390 to 420 °C). They are the highest temperature record of fluids in the Tiantangshan deposit. Chemically, the fluid inclusions in topaz are comparable to typical magmatic fluids in Rb/Na versus K/Na and Zn/Na versus K/Na (Fig. 10a, b; Shu et al. 2017, 2021; Mu et al. 2021) and have relatively high concentrations of Cs ($\bar{x}$ = 265 ppm), suggesting a genetic relation with the highly evolved alkali feldspar granite (Audétat et al. 2008; Audétat 2019). Importantly, these intermediate-density, high-temperature magmatic-derived fluids have relatively high concentrations of various ore elements (W, Sn, Rb, Pb, Zn, Fe, and Mn; Fig. 9; ESM Fig. S2), necessary to form the subsequent mineralization events.

The spatially coexisting wolframite and quartz (Qz_w-1) record different FIA (Fig. 6f, h), with fluid inclusions hosted in quartz having with lower Th and salinities than wolframite (Fig. 8a). This is also the case in many quartz-wolframite vein deposits (Campbell and Robinson-Cook 1987; Campbell and Panter 1990; Wei et al. 2012; Ni et al. 2015; Korges et al. 2018; Peng et al. 2018). It is noticed that the quartz in the vein (Qz_w-1) overgrows euhedral wolframite and fills in interspace among wolframite crystals (Figs. 4a and 6c, e). Therefore, the differences in fluid inclusion characteristics are attributed to earlier precipitation of wolframite than the coexisting quartz and evolution of the fluid during this stage of the paragenesis.

The W mineralizing fluid at Tiantangshan is therefore represented by the primary FIA in wolframite and topaz-hosted inclusions. The W concentration of the single-phase ID fluid falls from $\bar{x}$ = 23 ppm in topaz to mostly below detection limits ($\bar{x}$ = 1.2 ppm) in quartz from the biotite quartz veins (Fig. 9), likely due to wolframite precipitation. The precipitation mechanisms proposed for wolframite in other deposits include (1) fluid cooling (Ni et al. 2015; Codeço et al. 2017; Peng et al. 2018; Yang et al. 2019a), (2) fluid mixing (Wei et al. 2012; Legros et al. 2018; Pan et al. 2019), (3) decompression and phase separation of fluid (Korges et al. 2018; Pan et al. 2019), and (4) fluid-rock interaction (Lecumberri-Sanchez et al. 2017; Harlaux et al. 2021b). No significant changes in salinity or temperature are observed from topaz-hosted fluid inclusions to the primary FIAs in wolframite (Fig. 8a), suggesting that a decrease in temperature or fluid mixing was not involved in wolframite precipitation. Evidence of fluid boiling or immiscibility is also lacking in wolframite and topaz. Fluid-rock interaction is extensive in the system, as illustrated by the restricted distribution of W mineralization in greisen roof (Fig. 2d) and the tight association between wolframite and greisen alteration assemblages (Figs. 3e, f and 4a). The initial mineralizing fluid (topaz-hosted) contains Fe (and Mn) concentrations higher than W by two order magnitudes (ESM Table S3; Fig. 9), indicating that Fe or Mn leaching from the host rock (Lecumberri-Sanchez et al. 2017) is unnecessary in this case. Therefore, the most likely contribution of fluid-rock interaction to wolframite precipitation would be through greisenization causing an increase of the pH of the fluid (Halter et al. 1995, 1996, 1998) that caused wolframite precipitation (Wood and Samson 2000; Liu and Xiao 2020). The first generation of cassiterite (Cst I) volumetrically small and homogeneous in CL and microscopy (Fig. 6i) is also coeval with wolframite (Figs. 4a and 5). Decreasing Sn/Na + K ratios from the single-phase ID fluid hosted in topaz (greisen) to Qz_b-1 (Fig. 11a) likely relate to the precipitation of this early cassiterite. Therefore, the early Sn mineralization is also attributed to a pH increase (Heinrich 1990; Schmidt 2018), either through greisenization or biotite alteration of wallrocks.

Rubidium mineralization in the Tiantangshan deposit predominantly occurs as hydrothermal biotite in quartz veins hosted in volcanic rocks. The Rb mineralizing fluid is represented by the liquid-rich ID fluid inclusions in fluorite and FIAs in Qz_b-1 (Fig. 7b, d), which have relatively lower Th and salinities than those hosted in topaz and wolframite (Fig. 8a, b). The Rb and Cs concentrations, ratios to Na + K, and K/Na ratios are lower in biotite quartz veins than in the primary fluid inclusions in the greisen (Figs. 9, 10a, b, and 11a), suggesting that extensive depositions of hydrothermal biotite incorporated Rb (+Cs) and K from the fluids. The decreases in Rb and Cs (Fig. 9) are opposite of what would be expected as magma fractionates over time (Klemm et al. 2008; Audétat 2019). Since Rb and Cs are incorporated in significant amounts into biotite, they cannot be used as a fractionation indicator at Tiantangshan. Wolframite-cassiterite veins hosted in the greisen transition outwards to biotite quartz veins in the volcanic rocks proximal to the granite and to late and distal sphalerite-galena quartz veins. Noticeably, the single-phase ID fluids from the biotite quartz veins and the greisen have comparable Pb/(Na + K) and Zn/(Na + K) (Fig. 11b). These unchanged ratios indicate that Zn and Pb were conserved in fluids without significant deposition until later events at more distal locations, which further suggests that the single-phase fluid responsible for Rb mineralization is likely the same fluid with the initial single-phase ID fluid as it migrates outwards within the system. As the fluid migrates through the volcanic wallrocks, it forms biotite veins accompanied by extensive alteration of plagioclase to biotite in the trachyte-trachyandesite wallrocks (Figs. 3a, g and 4e), which host Rb mineralization. The Ca necessary to precipitate fluorite coeval to biotite (Fig. 4d) was likely derived from alteration of plagioclase to biotite. Given that Rb mineralization is limited to veins hosted in volcanic rocks with extensive alteration (Figs. 3a, g and 4d, e), a lithologic control is most likely.

Transitional-stage mineralization: Sn

Major Sn mineralization in the Tiantangshan deposit postdates early W-Rb-Sn mineralization. This stage of Sn mineralization is characterized by (1) cassiterite (Cst II) systematically overgrowing to coprecipitating with Qz-1 (Fig. 6d, i), (2) both cassiterite and quartz showing primary oscillatory zoning under CL (Fig. 6i), and (3) the thermometric properties of fluid inclusions hosted both in cassiterite and Qz-1 being similar (Figs. 6k, l and 8a, c). These observations indicate that cassiterite and intergrown quartz (Qz_w-1 and Qz_c-1) were simultaneously deposited and record the same fluid generation. Boiling FIAs coexisting with two-phase liquid-rich and vapor-rich fluid inclusions have been primarily identified in the cassiterite and intergrown quartz (Qz_w-1 and Qz_c-1) (Fig. 6f, k, l). The Sn concentration in the liquid-rich inclusions decreases significantly from prior paragenetic stages to mostly below detection limit (Fig. 9), illustrating precipitation of cassiterite. However, the liquid-rich inclusions in the boiling assemblages have a lower salinity than the early single-phase ID fluid (Fig. 8a, c). Boiling can lead to a decrease in trace element concentrations in the fluid either through loss of vapor or through precipitation of minerals, but due to the incompatible nature of chlorine with vapor and most minerals (Lecumberri-Sanchez and Bodnar 2018), significant boiling would cause an increase in salinity of the fluid inclusions (Heinrich et al. 2004; Driesner and Heinrich 2007; Audétat and Edmonds 2020). Alternatively, if the fluid was rich in volatiles (such as CO_2), the preferential volatile loss during immiscibility would keep the water salinity largely unmodified rather than decreasing. Therefore, the Th-salinity trajectory of the fluids cannot be explained exclusively by fluid boiling, and another simultaneous hydrothermal process was likely involved, which may be (1) fluid with lower salinity exsolved from a more fractionated magma or (2) mixing with an external fluid.

Fractional crystallization leads to fluids progressively more enriched in Rb and Cs (Klemm et al. 2008; Harlaux et al. 2017; Audétat 2019). As discussed above, Rb and Cs are incorporated in biotite and cannot be used as indicators of magmatic evolution in veins hosted within volcanic rocks. However, boiling assemblages in wolframite-cassiterite quartz veins hosted within greisen (unaffected by biotite precipitation) also show decreasing concentrations of Rb and Cs (Fig. 9), which seems to indicate that fractional crystallization is not the dominant process causing a salinity decrease.

The Th-salinity trend followed by fluids at Tiantangshan (Fig. 8) is characteristic of fluid mixing (Shu et al. 2017). Mixing with cold and dilute external fluids causes coupled cooling and dilution of the fluid system. Decompression triggered by fault extension likely caused fluid boiling and vein opening, which further resulted in external fluids entering the hydrothermal system along faults. The oscillatory zoning in both cassiterite and intergrown quartz (Qz_c-1 and Qz_w-1; Fig. 6i) might also support their precipitation under a condition of variable hydraulic pressure. Phase separation and fluid mixing could cause fluid oxidation, decrease in HCl activity, and dilution of the fluids (Drummond and Ohmoto 1985; Simonson and Palmer 1993; Schmidt 2018), all of which would destabilize Sn-chloride complexes and cause cassiterite precipitation (Heinrich 1990; Audétat et al. 1998; Korges et al. 2018; Schmidt 2018; Lehmann 2021).

Late mineralization: Pb–Zn

The Pb–Zn mineralization in the Tiantangshan deposit occurs distally along the F10-2 and F8 faults (Fig. 2). In the sphalerite-galena quartz vein, galena and sphalerite coprecipitate with Qz_s-2 and fluorite and postdate Qz_s-1 (Fig. 7f–h). The liquid-rich fluid inclusions in sphalerite (< 320 °C and salinity < 2 wt% $NaCl_{eq}$) have properties consistent with those in Qz_s-2 and fluorite (Fig. 8d). The sphalerite-galena quartz veins were likely derived from the early single-phase ID fluids evidenced by the similar Zn/(Na + K) and Pb/(Na + K) of fluids prior to Pb–Zn mineralization in the Qz_s-1 with those of the single-phase ID fluid in topaz of greisen and Qz_b-1 (Fig. 11b), which is also supported by their similar ratios of Rb vs. Na and Rb/(Na + K) vs. Cs/(Na + K) (Fig. 10c, d). The concurrent decreases in temperature, salinity, and Zn/(Na + K) and Pb/(Na + K) in late-stage fluids indicate precipitation of sphalerite and galena by fluid mixing (Figs. 8d and 11b; Shu et al. 2017). The fluids in this stage have similar Rb/(Na + K) vs. Cs/(Na + K) (Fig. 10d) and Rb vs. Na to the earlier fluid stages and unlike from formation waters (Fig. 10c), suggesting that the external fluid was meteoric water with little to no contribution of Rb and Cs (Shu et al. 2021). Meteoric water input into the system is also consistent with previous H–O isotopic results (Jia et al. 2018). Mixing with cold meteoric water could not only cause rapid cooling but also dilution of the magmatic fluids, which would destabilize the chloride complexes of Zn and Pb and cause metal precipitations (Fusswinkel et al. 2013; Brugger et al. 2016; Shu et al. 2017, 2021).

Genetic model: a two-endmember mixing model

Three stages of hydrothermal fluids formed the Tiantangshan deposit: (1) initial single-phase ID fluids exsolved from granitic magma responsible for W-Rb mineralization, (2) evolved magmatic fluids boiling combined mixing with meteoric water responsible for most Sn mineralization, and (3) extensive mixing with meteoric water responsible for Pb–Zn mineralization. These fluid stages are variably superimposed in the different quartz veins and mineralization (Figs. 6 and 7). The paragenetic sequence in all veins is similar, with some stages missing as a function of host rock

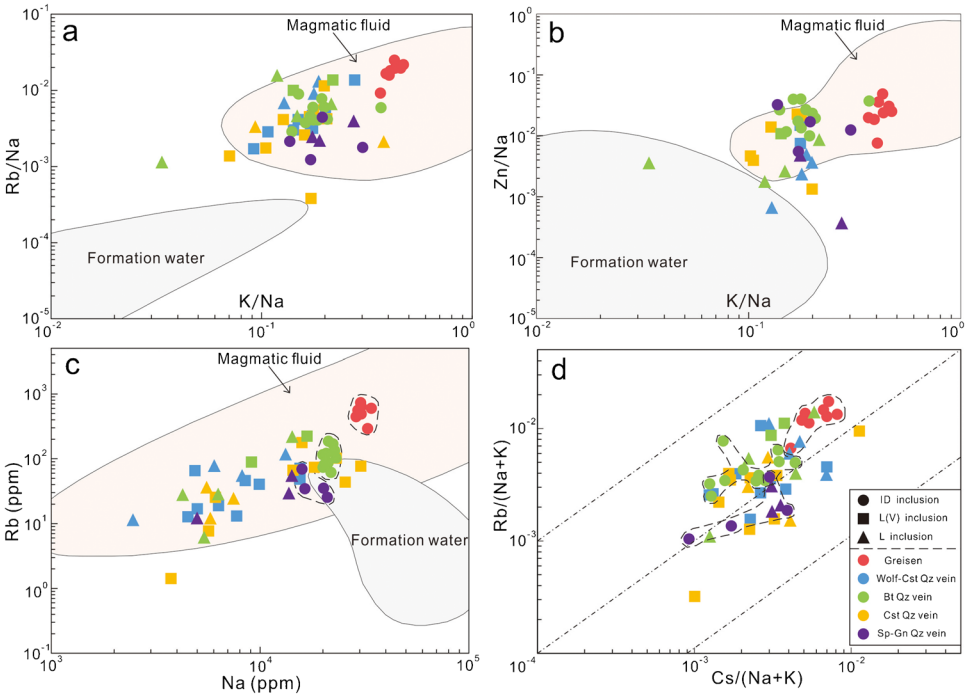

Fig. 10 Chemical plots of different stages of fluid inclusions from greisen and different quartz veins from the Tiantangshan deposit. **a** Rb/Na vs. K/Na. **b** Zn/Na vs. K/Na. **c** Rb vs. Na. **d** Rb/(Na + K) vs. Cs/(Na + K). The outlined region of magmatic fluid and formation water after Shu et al. (2017, 2021) and Mu et al. (2021). Fluid inclusion type: ID: liquid-rich intermediate-density inclusion, L(V): liquid-rich inclusion in boiling FIA, L: liquid-rich inclusion

and spatial distribution: early metal-hosted minerals (wolframite, cassiterite, and biotite) are crosscut, overgrown, or replaced by pyrite and magnetite and bismuthinite, lillianite, galena, sphalerite, chalcopyrite, and marcasite likely formed under the late fluid (Figs. 4 and 5). Such similarities further point to the different stages of fluids from the different quartz veins at the Tiantangshan deposit being derived from a single magmatic source, which is likely the alkali feldspar granite. The proportion of magmatic fluid progressively decreased and the meteoric water increased with time and outward migration, as shown by the Th-salinity trajectories and fluid chemistry (Figs. 8 and 9). The evolution of fluid properties in space and time is indicative of a mixing system including two endmember fluids. Magmatic metal-rich ID fluids altered the granite to form greisen in the roof and migrated into volcanic wallrocks along fissures or fractures (Fig. 12a) causing W-Rb-Sn mineralization (Fig. 12a). The high temperature and internal hydraulic pressure in this early stage likely prevented significant involvement of external fluids. Meteoric water started to infiltrate into the system along local decompression regions (fracture zones to greisen roof) and mixed with the local boiled magmatic fluid leading to the major Sn mineralization (Fig. 12b). Finally, the meteoric water became the dominant component in the hydrothermal fluids upon ongoing pressure release of the system. Dilution of the magmatic fluid caused Pb–Zn mineralization (Fig. 12c), which is extensively superimposed in all vein systems as shown by the fluid inclusions in prevalent secondary quartz (Qz_w-2, Qz_b-2, and Qz_c-2; Figs. 6e, j and 7a), and overprinting mineral assemblages (Bi sulfides, sphalerite, galena, chalcopyrite, and marcasite) in the different quartz veins (Figs. 4 and 5).

Conclusions

The polymetallic mineralization in the Tiantangshan deposit is zoned in space and time with (1) wolframite-cassiterite quartz veins hosted in the greisenized roof of granite and (2) biotite quartz veins (Rb mineralization), cassiterite quartz veins, and sphalerite-galena quartz veins progressively more distal and later hosted in surrounding volcanic wallrocks.

A three-stage evolution of hydrothermal fluids in the Tiantangshan deposit started by early high-temperature single-phase ID fluid exsolved from a granitic magma, which was responsible for the W-Sn-Rb mineralization. Precipitation of wolframite and cassiterite during this stage was caused by pH increase of the fluid through greisenization of granite, and the Rb-rich biotite precipitated through feldspar replacement in the volcanic wallrocks due to extensive fluid-rock interactions. The transitional stage consists of local boiling combined with fluid dilution and cooling by meteoric water, under which the major Sn mineralization formed, likely triggered by decompression events. The late fluids were dominated by meteoric water, and extensive fluid mixing contributed to the Pb–Zn mineralization. The hydrothermal fluids evolved from a single magmatic source, with the proportion of the magmatic fluid decreasing and that of meteoric water increasing in the fluid system with time and outward migration.

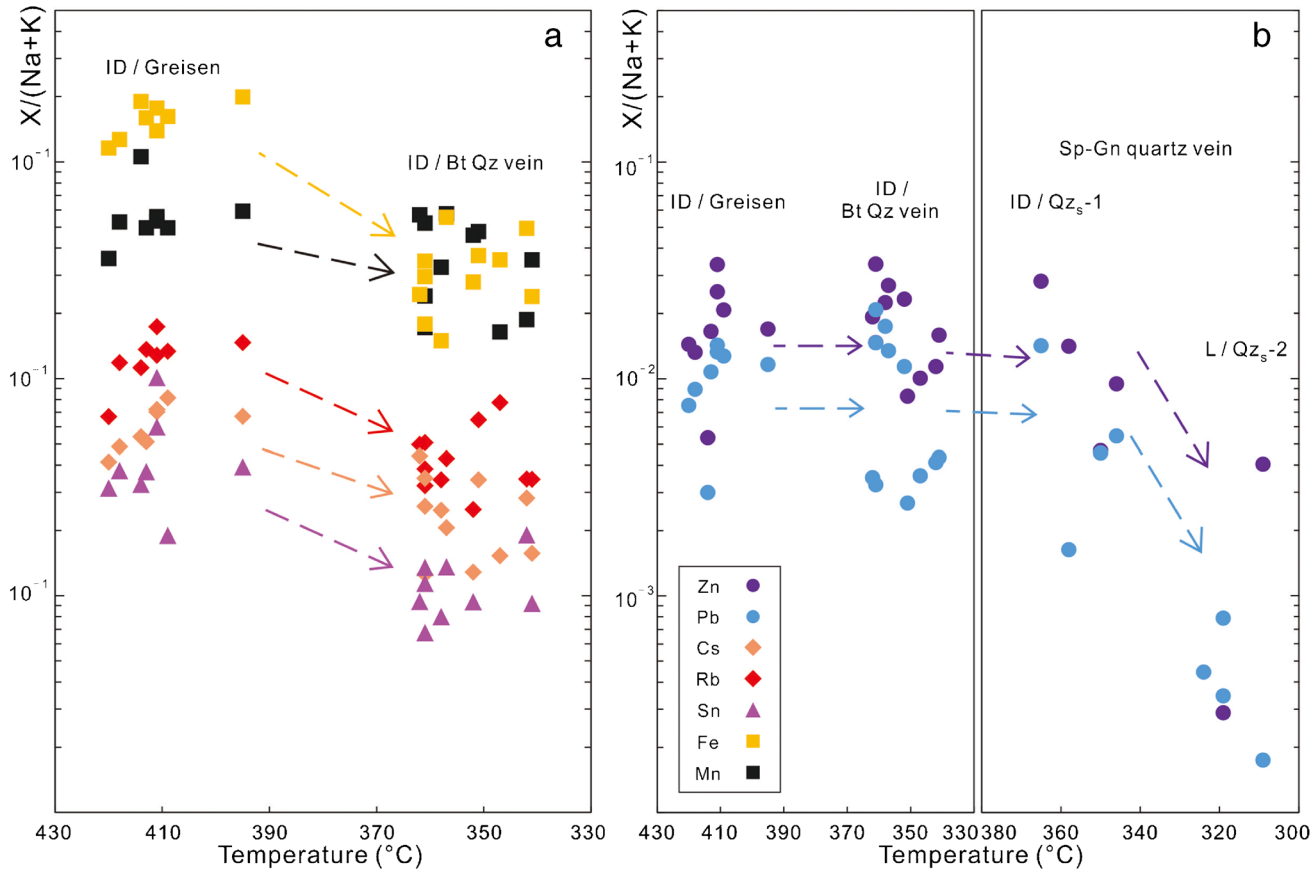

Fig. 11 Plot of Th vs. element/(Na + K). **a** Early single-phase ID fluid from greisen to biotite quartz vein. **b** Early single-phase ID fluid from greisen to biotite quartz vein, to early and late fluid in sphalerite-galena quartz vein. Fluid inclusion type: ID: liquid-rich intermediate-density inclusion, L: liquid-rich inclusion, Bt: biotite, Gn: galena, Qz: quartz, Sp: sphalerite

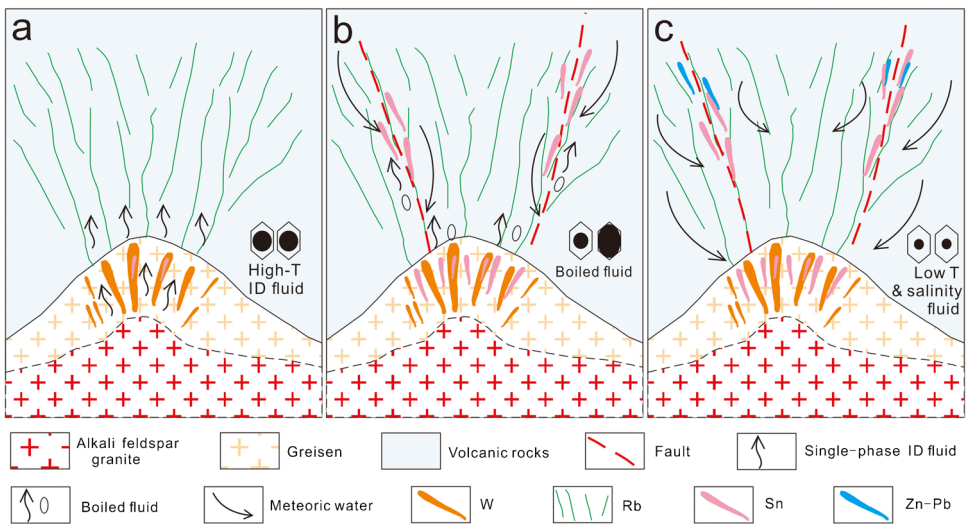

Fig. 12 Schematic illustration of the tempo-spatial evolution of the hydrothermal fluid and the polymetallic mineralization at Tiantangshan. **a** Early single-phase ID fluid exsolved from underlying granitic magma contributed to greisen and W-Sn mineralization at greisen roof and injected into volcanic wallrocks with extensive interaction to form Rb mineralization. **b** Local boiling occurred with infiltration of meteoric water due to decompression to account for the major Sn mineralization. **c** Extensive fluid mixing by meteoric water leading to Pb–Zn mineralization at distal regions

Supplementary Information The online version contains supplementary material available at https://doi.org/10.1007/s00126-022-01155-7.

Acknowledgements We thank Dr. Yan-Wen Tang for his help in LA-ICP-MS analyses of fluid inclusions. We are indebted to Prof. Tian-Zhu Ye and staff of the Guangdong Mining Corporation for their indispensable help in the field works. We thank Editor-in-Chief Georges Beaudoin, Associated Editor Mohammed Bouhabdellah, Matthieu Harlaux, and Gilles Levresse for providing constructive comments to earlier versions of this manuscript.

Funding This study was financially supported by the National Key Research and Development Program of China (Grant No. 2018YFA0702603).

Declarations

Conflict of interest The authors declare no competing interests.

References

Audétat A (2019) The metal content of magmatic-hydrothermal fluids and its relationship to mineralization potential. Econ Geol 114:1033–1056

Audétat A, Edmonds M (2020) Magmatic-hydrothermal fluids. Elements 16:401–406

Audétat A, Günther D, Heinrich CA (1998) Formation of a magmatic-hydrothermal ore deposit: insights with LA-ICP-MS analysis of fluid inclusions. Science 279:2091–2094

Audétat A, Pettke T, Heinrich CA, Bodnar RJ (2008) The composition of magmatic-hydrothermal fluids in barren and mineralized intrusions. Econ Geol 103:877–908

Brugger J, Liu WH, Etschmann B, Mei Y, Sherman DM, Testemale D (2016) A review of the coordination chemistry of hydrothermal systems, or do coordination changes make ore deposits? Chem Geol 447:219–253

Campbell AR, Panter KS (1990) Comparison of fluid inclusion in coexisting (cogenetic) wolframite, cassiterite and quartz from St. Michaels Mount and Cligga Head, Cornwall. England Geochim Cosmochim Acta 54:673–681

Campbell AR, Robinson-Cook S (1987) Infrared fluid inclusion microthermometry on coexisting wolframite and quartz. Econ Geol 82:1640–1645

Casanova V, Kouzmanov K, Audétat A, Wälle M, Ubrig N, Ortelli M, Fontboté L (2018) Fluid inclusion studies in opaque ore minerals: II. A comparative study of synthetic fluid inclusions hosted in quartz and opaque minerals. Econ Geol 113:1861–1883

Černý P, Blevin PL, Cuney M, London D (2005) Granite-related ore deposits. In: Hedenquist JW, Thompson JFH, Goldfarb RJ, Richards JP (eds) Economic Geology—One hundredth anniversary volume, 1905–2005: Littleton. Society of Economic Geologists, Colo., pp 337–370

Codeço MS, Weis P, Trumbull RB, Pinto F, Lecumberri-Sanchez P, Wilke FDH (2017) Chemical and boron isotopic composition of hydrothermal tourmaline from the Panasqueira W-Sn-Cu deposit, Portugal. Chem Geol 468:1–16

Driesner T, Heinrich CA (2007) The system H2O-NaCl. Part I: correlation formulae for phase relations in temperature-pressure-composition space from 0 to 1000°C, 0 to 5000 bar, and 0 to 1 X_{NaCl}. Geochim Cosmochim Acta 71:4880–4901

Drummond SE, Ohmoto H (1985) Chemical evolution and mineral deposition in boiling hydrothermal systems. Econ Geol 80:126–147

Fusswinkel T, Wagner T, Wälle M, Wenzel T, Heinrich CA, Markl G (2013) Fluid mixing forms basement-hosted Pb-Zn deposits: insight from metal and halogen geochemistry of individual fluid inclusions. Geology 41:679–682

Goldstein RH, Reynolds TJ (1994) Systematics of fluid inclusions in diagenetic minerals. In: Society of Sedimentary Geology, SEPM Short Course, 1–199

Guillong M, Meier DL, Allan MM, Heinrich CA, Yardley BWD (2008) SILLS: A MATLAB-based program for the reduction of laser ablation ICP-MS data of homogeneous materials and inclusions. In: Sylvester, P. (Ed.), Laser Ablation ICP-MS in the Earth Sciences: Current Practices and Outstanding Issues: Mineralogical Association of Canada Short Course Series 40: 328–333

Guo YQ (2009) Study on geology and elemental chemistry of the Jinshizhang epithermal silver polymetallic deposit in northern Guangdong, China: Master thesis, China University of Geosciences (Beijing), 1–83 (in Chinese with English abstract)

Halter WE, Williams-Jones AE, Kontak DJ (1995) Origin and evolution of the greisenizing fluid at the East Kemptville tin deposit, Nova Scotia, Canada. Econ Geol 93:1036–1051

Halter WE, Williams-Jones AE, Kontak DJ (1996) The role of greisenization in cassiterite precipitation at the East Kemptville tin deposit, Yarmouth County, Nova Scotia. Econ Geol 91:368–385

Halter WE, Williams-Jones AE, Kontak DJ (1998) Modeling fluid–rock interaction during greisenization at the East Kemptville tin deposit: implications for mineralization. Chem Geol 150:1–17

Han JS, Chen HY, Hollings P, Wang J, Zhang DX, Zhang L, Zeng T, Ma JL, Ai YM (2021) Efficient enrichment of Rb during the magmatic-hydrothermal transition in a highly evolved granitic system: implications from mica chemistry of the Tiantangshan Rb-Sn-W deposit. Chem Geol 560:120020

Harlaux M, Mercadier J, Bonzi WME, Kremer V, Marignac C, Cuney M (2017) Geochemical signature of magmatic-hydrothermal fluids exsolved from the Beauvoir rare-metal granite (Massif Central, France): insights from LA-ICPMS analysis of primary fluid inclusions. Geofluids 2017:1925817

Harlaux M, Kouzmanov K, Gialli S, Marger K, Bouvier AS, Baumgartner LP, Rielli A, Dini A, Chauvet A, Kalinaj M, Fontboté L (2021) Fluid mixing as primary trigger for cassiterite deposition: evidence from in situ δ^{18}O-δ^{11}B analysis of tourmaline from the world-class San Rafael tin (-copper) deposit. Peru Earth Planet Sci Lett 563:116889

Harlaux M, Marignac C, Mercadier J, Poujol M, Boiron MC, Kouzmanov K, Camacho A, Alikouss S, Roméo B, Mouthier B, Cuney M (2021) Multistage development of a hydrothermal W deposit during the Variscan late-orogenic evolution: the Puy-les-Vignes breccia pipe (Massif Central, France). BSGF-Earth Sci Bull 192:33

Heinrich CA (1990) The chemistry of hydrothermal tin(-tungsten) ore deposition. Econ Geol 85:457–481

Heinrich CA, Pettke T, Halter WE, Aigner-Torres M, Audétat A, Gunther D, Hanttendorf B, Bleiner D, Guillong M, Horn I (2003) Quantitative multi-element analysis of minerals, fluid, and melt inclusions by laser ablation-inductively coupled plasma-mass spectrometry. Geochim Cosmochim Acta 67:3473–3496

Heinrich CA, Driesner T, Stefánsson A, Seward TM (2004) Magmatic vapor contraction and the transport of gold from the porphyry environment to epithermal ore deposits. Geology 32:761–764

Jia HX, Pang ZS, Chen RY, Xue JL, Chen H, Lin LJ (2018) Genesis and hydrothermal evolution of the Tiantangshan tin-polymetallic

deposit, south-eastern Nanling Range, South China. Geol J 54:3958–3979

Jia RY, Wang GC, Geng L, Pang ZS, Jia HX, Zhang ZH, Chen H, Liu Z (2019) Petrogenesis of the early Cretaceous Tiantangshan A-type granite, Cathaysia block, SE China: implication for the tin mineralization. Minerals 9:257

Kamilli RJ, Kimball BE, Carlin JFJ (2017) Tin: chap. S of Schulz, K.J., DeYoung, J.H., Jr., Seal, R.R., II, and Bradley, D.C., eds., Critical mineral resources of the United States—economic and environmental geology and prospects for future supply. U.S. Geological Survey Professional Paper 1802, S1– S53

Klemm LM, Pettke T, Heinrich CA (2008) Fluid and source magma evolution of the Questa porphyry Mo deposit, New Mexico, USA. Mineral Deposita 43:533–552

Korges M, Weis P, Lüders V, Laurent O (2018) Depressurization and boiling of a single magmatic fluid as a mechanism for tin-tungsten deposit formation. Geology 46:75–78

Lan TG, Hu RZ, Fan HR, Bi XW, Tang YW, Zhou L, Mao W, Chen YH (2017) In-situ analysis of major and trace elements in fluid inclusion and quartz: LA-ICP-MS method and applications to ore deposits. Acta Petrol Sin 33:3239–3262 (in Chinese with English abstract)

Lan TG, Hu RZ, Bi XW, Mao GJ, Wen BJ, Liu L, Chen YH (2018) Metasomatized asthenospheric mantle contributing to the generation of Cu-Mo deposits within an intracontinental setting: a case study of the similar to 128 Ma Wangjiazhuang Cu-Mo deposit, eastern North China craton. J Asian Earth Sci 160:460–489

Landtwing MR, Pettke T, Halter WE, Heinrich CA, Redmond PB, Einaudi MT, Kunze K (2005) Copper deposition during quartz dissolution by cooling magmatic–hydrothermal fluids: the Bingham porphyry. Earth Planet Sci Lett 235:229–243

Lecumberri-Sanchez P, Vieira R, Heinrich CA, Pinto F, Wälle M (2017) Fluid-rock interaction is decisive for the formation of tungsten deposits. Geology 45:579–582

Lecumberri-Sanchez P, Bodnar RJ (2018) Halogen geochemistry of ore deposits: contributions towards understanding sources and processes. In: Aranovich, L., and Harlov, D. (Eds.) The Role of Halogens in Terrestrial and Extraterrestrial Geochemical Processes: Surface, Crust, and Mantle, Springer Geochemistry, 261–305

Legros H, Richard A, Tarantola A, Kouzmanov K, Mercadier J, Vennemann T, Marignac C, Cuney M, Wang RC, Charles N, Bailly L, Lespinasse MY (2018) Multiple fluids involved in granite-related W-Sn deposits from the world-class Jiangxi province (China). Chem Geol 508:92–115

Legros H, Lecumberri-Sanchez P, Elongo V, Laurent O, Falck H, Adlakha E, Chelle-Michou C (2020) Fluid evolution of the Cantung tungsten skarn, Northwest Territories, Canada: differentiation and fluid-rock interaction. Ore Geol Rev 127:103866

Legros H, Harlaux M, Mercadier J, Romer RL, Poujol M, Camacho A, Marignac C, Cuney M, Wang RC, Charles N, Lespinasse MY (2020) The world-class Nanling metallogenic belt (Jiangxi, China): W and Sn deposition at 160 Ma followed by 30 my of hydrothermal metal redistribution. Ore Geol Rev 117:103302

Lehmann B (1990) Metallogeny of tin. Springer, Berlin, pp 1–211

Lehmann B (2021) Formation of tin ore deposits: a reassessment. Lithos 402–403:105756

Li ZX, Li XH (2007) Formation of the 1300 km-wide intra-continental orogen and post orogenic magmatic province in Mesozoic South China: a flat-slab subduction model. Geology 35:179–182

Liu XC, Xiao CH (2020) Wolframite solubility and precipitation in hydrothermal fluids: Insight from thermodynamic modeling. Ore Geol Rev 117:103289

Liu P, Mao JW, Santosh M, Xu LG, Zhang RQ, Jia LH (2018) The Xiling Sn deposit, eastern Guangdong Province, Southeast China: a new genetic model from $^{40}Ar/^{39}Ar$ muscovite and U-Pb cassiterite and zircon geochronology. Econ Geol 113:511–530

Liu P, Mao JW, Jian W, Mathur R (2020) Fluid mixing leads to mainstage cassiterite precipitation at the Xiling Sn polymetallic deposit, SE China: evidence from fluid inclusions and multiple stable isotopes (H–O–S). Mineral Deposita 55:1233–1246

Liu P, Mao JW, Lehmann B, Peng LL, Zhang RQ, Wang FY, Lu GA, Jiang CY (2021) Cassiterite U-Pb dating of the lower Cretaceous Yanbei tin porphyry district in the Mikengshan volcanic basin. SE China Ore Geol Rev 134:104151

Mao JW, Cheng YB, Chen MH, Pirajno F (2013) Major types and time–space distribution of Mesozoic ore deposits in South China and their geodynamic settings. Mineral Deposita 48:267–294

Moritz R (2006) Fluid salinities obtained by infrared microthennometry of opaque minerals: implications for ore deposit modeling–a note of caution. J Geochem Explor 89:284–287

Mu L, Hu RZ, Bi XW, Tang YY, Lan TG, Lan Q, Zhu JJ, Peng JT, Oyebamiji A (2021) New insights into the origin of the world-class Jinding sediment-hosted Zn-Pb deposit, southwestern China: evidence from LA-ICP-MS analysis of individual fluid inclusions. Econ Geol 116:883–907

Ni P, Wang XD, Wang GG, Huang JB, Pan JY, Wang TG (2015) An infrared microthermometric study of fluid inclusions in coexisting quartz and wolframite from Late Mesozoic tungsten deposits in the Gannan metallogenic belt, South China. Ore Geol Rev 65:1062–1077

Ni P, Li WS, Pan JY (2020) Ore-forming fluid and metallogenic mechanism of wolframite-quartz vein-type tungsten deposits in South China. Acta Geol Sin (english Edition) 94:1774–1796

Ni P, Wang GG, Li WS, Chi Z, Li SN, Gao Y (2021) A review of the Yanshanian ore-related felsic magmatism and tectonic settings in the Nanling W-Sn and Wuyi Au-Cu metallogenic belts, Cathaysia Block. South China Ore Geol Rev 133:104088

Pan JY, Ni P, Wang RC (2019) Comparison of fluid processes in coexisting wolframite and quartz from a giant vein-type tungsten deposit, South China: insights from detailed petrography and LA-ICP-MS analysis of fluid inclusions. Am Mineral 104:1092–1116

Peng NJ, Jiang SY, Xiong SF, Pi DH (2018) Fluid evolution and ore genesis of the Dalingshang deposit, Dahutang W-Cu ore field, northern Jiangxi Province, South China. Mineral Deposita 53:1079–1094

Peng HW, Fan HR, Santosh M, Hu FF, Jiang P (2020) Infrared microthermometry of fluid inclusions in transparent to opaque minerals: challenges and new insights. Mineral Deposita 55:1425–1440

Peng HW, Fan HR, Jiang P, Hu HL, Lan TG (2021) Two-stage rollbacks of the paleo-Pacific plate beneath the Cathaysia block during Cretaceous: insights from A-type granites and volcanic rocks. Gondwana Res 97:158–175

Peng HW, Fan HR, Zhang RQ, Lan TG (2021) Geochronological framework and ore genesis of the Tiantangshan Rb-Sn-W deposit, northeastern Guangdong, south China: Constraints from cassiterite and monazite U-Pb dating. Ore Geol Rev 139:104457

Ramboz C, Schnapper D, Dubessy J (1985) The P-V-T-X-f_{O2}-CH_4-bearing fluid in a wolframite vein: reconstruction from fluid inclusion studies. Geochim Cosmochim Acta 48:205–219

Romer RL, Kroner U (2016) Phanerozoic tin and tungsten mineralization–tectonic controls on the distribution of enriched protoliths and heat sources for crustal melting. Gondwana Res 31:60–95

Rottier B, Kouzmanov K, Casanova V, Wälle M, Fontboté L (2018) Cyclic dilution of magmatic metal-rich hypersaline fluids by magmatic low-salinity fluid: a major process generating the giant epithermal polymetallic deposit of Cerro de Pasco, Peru. Econ Geol 113:825–856

Samson IM (1990) Fluid evolution and mineralization in a subvolcanic granite stock: the Mount Pleasant W-Mo-Sn deposits, New Brunswick, Canada. Econ Geol 85:145–163

Schmidt C (2018) Formation of hydrothermal tin deposits: Raman spectroscopic evidence for an important role of aqueous Sn (IV) species. Geochim Cosmochim Acta 220:499–511

Shu QH, Chang ZS, Hammerli J, Lai Y, Huizenga J (2017) Composition and evolution of fluids forming the Baiyinnuo'er Zn-Pb skarn deposit, northeastern China: insights from laser ablation ICP-MS study of fluid inclusions. Econ Geol 112:1441–1460

Shu QH, Chang ZS, Mavrogenes J (2021) Fluid compositions reveal fluid nature, metal deposition mechanisms, and mineralization potential: an example at the Haobugao Zn-Pb skarn, China. Geology 49:473–477

Simonson JM, Palmer DA (1993) Liquid-vapor partitioning of HCl (aq) to 350°C. Geochim Cosmochim Acta 57:1–7

Steele-MacInnis M, Lecumberri-Sanchez P, Bodnar RJ (2012) Short note: HokieFlincs_H2O-NaCl: a Microsoft Excel spreadsheet for interpreting microthermometric data from fluid inclusions based on the PVTX properties of H2O-NaCl. Comput Geosci 49:334–337

Sun Y, Wang DH, Wang CH, Li JK, Zhao Z, Wang Y, Guo WM (2019) Metallogenic regularity, new prospecting and guide direction of rubidium deposits in China. Acta Geol Sin 93:1231–1244 (in Chinese with English abstract)

Tang Y, Cui K, Zheng Z, Gao J, Han J, Yang J, Liu L (2020) LA-ICP-MS U-Pb geochronology of wolframite by combining NIST series and common lead-bearing MTM as the primary reference material: implications for metallogenesis of South China. Gondwana Res 83:217–231

Wang DH, Fan H, Wang Y, He HH, Li XM, Liu XX, Sheng JF, Liang T (2020) Regional metallogeny of tungsten-tin-polymetallic deposits in Nanling region. South China Ore Geol Rev 120:103305

Wei WF, Hu RZ, Bi XW, Peng JT, Su WC, Song SQ, Shi SH (2012) Infrared microthermometric and stable isotopic study of fluid inclusions in wolframite at the Xihuashan tungsten deposit, Jiangxi province, China. Mineral Deposita 47:589–601

Werner ABT, Sinclair WD, Amey EB (2014) International strategic mineral issues summary report—Tungsten. U.S. Geological Survey Circular 930–O, 1–74

Wilkinson (1990) The role of metamorphic fluids in the development of the Cornubian Orefield: fluid inclusion evidence from south Cornwall. Mineral Mag 54:219–230

Wilkinson JJ (2001) Fluid inclusions in hydrothermal ore deposits. Lithos 65:229–272

Wood SA, Samson IM (2000) The hydrothermal geochemistry of tungsten in granitoid environments: I. Relative solubilities of ferberite and scheelite as a function of T, P, pH, and mNaCl. Econ Geol 95:143–182

Yang JH, Kang LF, Liu L, Peng JT, Qi YQ (2019) Tracing the origin of ore-forming fluids in the Piaotang tungsten deposit, South China: constraints from in-situ analyses of wolframite and individual fluid inclusion. Ore Geol Rev 111:102939

Yang JH, Zhang Z, Peng JT, Liu L, Leng CB (2019) Metal source and wolframite precipitation process at the Xihuashan tungsten deposit, South China: insights from mineralogy, fluid inclusion and stable isotope. Ore Geol Rev 111:102965

Yuan SD, Williams-Jones AE, Romer RL, Zhao PL, Mao JW (2019) Protolith-related thermal controls on the decoupling of Sn and W in Sn-W metallogenic provinces: insights from the Nanling region, China. Econ Geol 114:1005–1012

Zhao GC, Cawood PA (2012) Precambrian geology of China. Precambrian Res 222–223:13–54

Zhou XM, Sun T, Shen WZ, Shu LS, Niu YL (2006) Petrogenesis of Mesozoic granitoids and volcanic rocks in South China: a response to tectonic evolution. Episodes 29:26–33